

# AD-A231 735 CITATION PAGE

Form Approved  
OMB No. 0704-0188

1

ed to average 1 hour per response, including the time for reviewing instructions, searching existing data sources, gathering and maintaining the data needed, and completing and reviewing the collection of information. Send comments regarding this burden estimate or any other aspect of this collection of information, including suggestions for reducing this burden, to Washington Headquarters Services, Directorate for Information Operations and Reports, 1215 Jefferson Davis Highway, Suite 1204, Arlington, VA 22202-4302, and to the Office of Management and Budget, Paperwork Reduction Project (0704-0188), Washington, DC 20503

1. AGENCY USE ONLY (Leave blank)		2. REPORT DATE 1990	3. REPORT TYPE AND DATES COVERED Thesis/Dissertation	
4. TITLE AND SUBTITLE Controller Design for a Laser Steering Mirror on a Flexible Structure			5. FUNDING NUMBERS	
6. AUTHOR(S) Richard J. Adams				
7. PERFORMING ORGANIZATION NAME(S) AND ADDRESS(ES) AFIT Student at: University of Washington			8. PERFORMING ORGANIZATION REPORT NUMBER AFIT/CI/CIA - 90-135	
9. SPONSORING/MONITORING AGENCY NAME(S) AND ADDRESS(ES) AFIT/CI Wright-Ptatterson AFB OH 45433			10. SPONSORING/MONITORING AGENCY REPORT NUMBER	
11. SUPPLEMENTARY NOTES				
12a. DISTRIBUTION/AVAILABILITY STATEMENT Approved for Public Release IAW AFR 190-1 Distribution Unlimited ERNEST A. HAYGOOD, 1st Lt, USAF Executive Officer, Civilian Institution Programs			12b. DISTRIBUTION CODE	
13. ABSTRACT (Maximum 200 words)				
				
14. SUBJECT TERMS			15. NUMBER OF PAGES 54	
			16. PRICE CODE	
17. SECURITY CLASSIFICATION OF REPORT UNCLASSIFIED	18. SECURITY CLASSIFICATION OF THIS PAGE	19. SECURITY CLASSIFICATION OF ABSTRACT	20. LIMITATION OF ABSTRACT	

Controller Design for a Laser Steering Mirror on a  
Flexible Structure

by Richard J. Adams, 2nd Lt. USAF

1990

54 pages ( 44 pages in body )

A thesis submitted in partial fulfillment  
of the requirements for the degree of

Master of Science in Aeronautics and Astronautics

University of Washington, Seattle

**91 2 06 095**

University of Washington

Abstract

# Controller Design for a Laser Steering Mirror on a Flexible Structure

by Richard J. Adams

Chairperson of Supervisory Committee:

Prof. Juris Vagners

Dept. of Aeronautics and Astronautics

An experimental setup for disturbance rejection and pointing for a structurally borne laser beam path is explored. Motivation for the experiment is the expanding demand for structurally mounted pointing systems in space applications. The design and implementation of a disturbance rejection system is manifested in the form of a proportional-integral and feedforward controlled piezo actuated mirror. Good line-of-sight structural disturbance rejection is demonstrated for the primary transverse flexible modes of a 20 bay, 7.07 meter long, planar truss structure. A bandwidth of 60 Hz is achieved for the closed loop mirror-piezo plant. Two beam pointing systems are explored using a DC motor driven turntable to provide large scale angular movement. The actuation methods are coupled, using the turntable as a single axis gimbal for slow pointing, and the piezo-mirror in a fast disturbance rejection, fine pointing loop. Theoretical design and practical hardware considerations are explored and future research possibilities examined.



Accession For	
NTIS GRA&I	<input checked="" type="checkbox"/>
DTIC TAB	<input type="checkbox"/>
Unannounced	<input type="checkbox"/>
Justification	
By	
Distribution/	
Availability Codes	
Dist	Avail and/or Special
A-1	

Controller Design for a Laser Steering Mirror on a Flexible  
Structure

by

Richard J. Adams

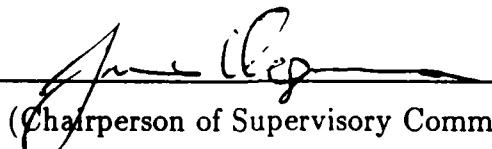
A thesis submitted in partial fulfillment  
of the requirements for the degree of

Master of Science in Aeronautics and Astronautics

University of Washington

1990

Approved by \_\_\_\_\_

  
(Chairperson of Supervisory Committee)

Program Authorized

to Offer Degree \_\_\_\_\_

Department of Aeronautics & Astronautics

Date \_\_\_\_\_

December 5, 1990

In presenting this thesis in partial fulfillment of the requirements for the Master's degree at the University of Washington, I agree that the Library shall make its copies freely available for inspection. I further agree that extensive copying of this thesis is allowable only for scholarly purposes, consistent with "fair use" as prescribed in the U. S. Copyright Law. Any other reproduction for any purposes or by any means shall not be allowed without my written permission.

Signature Richard J. Allen

Date 5 DEC 90

University of Washington

Abstract

## Controller Design for a Laser Steering Mirror on a Flexible Structure

by Richard J. Adams

Chairperson of Supervisory Committee:

Prof. Juris Vagners

Dept. of Aeronautics and Astronautics

An experimental setup for disturbance rejection and pointing for a structurally borne laser beam path is explored. Motivation for the experiment is the expanding demand for structurally mounted pointing systems in space applications. The design and implementation of a disturbance rejection system is manifested in the form of a proportional-integral and feedforward controlled piezo actuated mirror. Good line-of-sight structural disturbance rejection is demonstrated for the primary transverse flexible modes of a 20 bay, 7.07 meter long, planar truss structure. A bandwidth of 60 Hz is achieved for the closed loop mirror-piezo plant. Two beam pointing systems are explored using a DC motor driven turntable to provide large scale angular movement. The actuation methods are coupled, using the turntable as a single axis gimbal for slow pointing, and the piezo-mirror in a fast disturbance rejection, fine pointing loop. Theoretical design and practical hardware considerations are explored and future research possibilities examined.

## TABLE OF CONTENTS

<b>List of Figures</b>	iv
<b>List of Tables</b>	vi
<b>Chapter 1 Introduction</b>	<b>1</b>
1.1 Background . . . . .	1
1.2 Problem Definition . . . . .	1
1.3 Hardware Description . . . . .	4
1.3.1 Truss . . . . .	4
1.3.2 Laser . . . . .	4
1.3.3 Optics . . . . .	4
1.3.4 Piezo Actuators/Mirror Mounts . . . . .	4
1.3.5 Photodetectors . . . . .	6
1.3.6 Accelerometer . . . . .	7
1.3.7 Proof Mass Actuators/Air Jet Thrusters . . . . .	8
1.3.8 Analog Computers . . . . .	9
1.3.9 Fourier Analyzer . . . . .	9
<b>Chapter 2 Modeling and Control Theory</b>	<b>12</b>
2.1 Actuated Mirror Modeling . . . . .	12
2.1.1 Model Structure . . . . .	12
2.1.2 Experimental Development . . . . .	13
2.2 Controller Design . . . . .	14
2.2.1 Closed Loop Design . . . . .	14
2.2.2 Feedforward Design . . . . .	16
<b>Chapter 3 Experimental Results</b>	<b>19</b>
3.1 Design Limitations . . . . .	19
3.2 Final Controller Selection . . . . .	20

3.2.1	PI Controller . . . . .	20
3.2.2	Feedforward Controller . . . . .	22
3.3	Command Following and Noise Rejection . . . . .	25
3.4	Disturbance Rejection . . . . .	27
<b>Chapter 4</b>	<b>Laser Pointing Systems</b>	<b>31</b>
4.1	Introduction . . . . .	31
4.2	Description of Hardware . . . . .	31
4.2.1	DC Motor Driven Turntable . . . . .	31
4.2.2	Displacement Transducer . . . . .	33
4.3	Modeling of the DC Motor Driven Turntable . . . . .	33
4.4	Lead Compensation . . . . .	36
4.5	Command Driven Pointing System . . . . .	37
4.6	Master-Slave Pointing System . . . . .	40
<b>Chapter 5</b>	<b>Conclusions and Recommendations for Future Work</b>	<b>44</b>
	<b>Bibliography</b>	<b>45</b>

## LIST OF FIGURES

1.1	Experimental Setup . . . . .	2
1.2	Arrangement of Experimental Hardware . . . . .	3
1.3	Mirror-Piezo Plant . . . . .	5
1.4	Power Spectrum of Sensor Noise . . . . .	6
1.5	Power Spectrum of Sensor Noise with <i>Black Box</i> . . . . .	7
1.6	Tip Mounted Proof Mass Actuator and Air Jet Thrusters . . . . .	8
1.7	Tek 2630 Fourier Analyzer and Zenith 248 AT Data Acquisition Setup . . . . .	10
2.1	Mirror-Piezo Layout . . . . .	12
2.2	Experimental and Theoretical Mirror-Piezo $V_{sens}/V_{control}$ . . . . .	14
2.3	Unity Feedback Block Diagram . . . . .	15
2.4	Feedforward Control Block Diagram . . . . .	17
3.1	Block Diagram of Overall Control Structure . . . . .	20
3.2	Magnitude Plot of PI Controller, $K(s)$ . . . . .	21
3.3	Magnitude Plot of the Forward Transfer Function $K(s)G(s)$ . . . . .	22
3.4	Circuit Diagram of PI Controller . . . . .	23
3.5	Circuit Diagram of Approximate Integrator . . . . .	24
3.6	Experimental and Theoretical $V_{sensor}/V_{reference}$ of the Closed Loop System . . . . .	25
3.7	Sine Sweep of $V_{sensor}/V_{reference}$ for Closed Loop System . . . . .	26
3.8	$V_{sensor}/V_{PMA}$ for OL(-), OL FF(--), CL(-.), and CL FF(···) . . . . .	27
3.9	Structural Disturbance Rejection from Acquired Data . . . . .	29
4.1	Dual Actuator Setup for Mirror Pointing . . . . .	32
4.2	Experimental Root Locus for Turntable . . . . .	34
4.3	Open Loop Turntable Step Response . . . . .	36
4.4	Closed Loop Turntable Step Response . . . . .	37
4.5	Command Driven Pointing System Block Diagram . . . . .	39

4.6 Master-Slave Pointing System Block Diagram . . . . . 41

4.7 Piezo Loop PI Controller Output Voltage Response to Step Target  
Displacement . . . . . 42

## LIST OF TABLES

3.1 Discrete Disturbance Rejection Values in dB . . . . .	29
---	----

## ACKNOWLEDGMENTS

The author would like to express appreciation to those at the U.S. Air Force Academy who were so instrumental in making the experiment happen: DFAS, Lt. Col. Waggle, and Captain Scott Trimboli for the support and funding, DFEM and Captain Steve Webb for technical support and use of the lab facilities, and F.J. Seiler Labs and Hugh Ward for assistance with the optical setup. Special thanks to Mr. Jim Smith of F.J. Seiler Labs for his time and technical expertise, he is the man who made the pieces of the puzzle fit. Also special thanks to Major Ken Barker who gave me the topic, got me started, and guided me along the way.

## Chapter 1

# INTRODUCTION

### *1.1 Background*

A number of expanding areas in space technology are creating a demand for highly accurate, high bandwidth pointing systems. They include communications systems, payload pointing systems for the shuttle and space station, astronomical systems, and directed energy systems for the Space Defense Initiative. In all of these systems, pointing accuracy is to some degree susceptible to vibrations due to the excitation of flexible structural modes of the supporting structure. Sources of excitation in space structures include asymmetric solar heating, micro-meteorite impacts, spacecraft maneuvering, and routine onboard operations such as crew movement, pump vibrations, and radiator motions [Hughes 86]. The problem of dealing with these disturbances to a pointing system is the primary focus of this research. Other non-structural disturbances of interest are atmospheric interference, laser beam jitter, and small scale high speed target maneuvering. The disturbance rejection pointing system explored in this research represents a high bandwidth, low degree of freedom controller which, when paired with a slower, high degree of freedom gimbal system, make up a complete pointing system. The final topic in this research is an examination of some simple control laws that coordinate the efforts of these fast and slow loops.

### *1.2 Problem Definition*

In the experiment setup shown in Figure 1.1, beam path optics are mounted on a flexible planar truss structure to simulate the modal excitations found in the space platform environment. A laser beam is directed from the source, to a mirror mounted at the base of the truss, to a mirror mounted at the tip of the structure, through a beam splitter, and finally through a cylindrical lens and into a single axis linear photodetector.

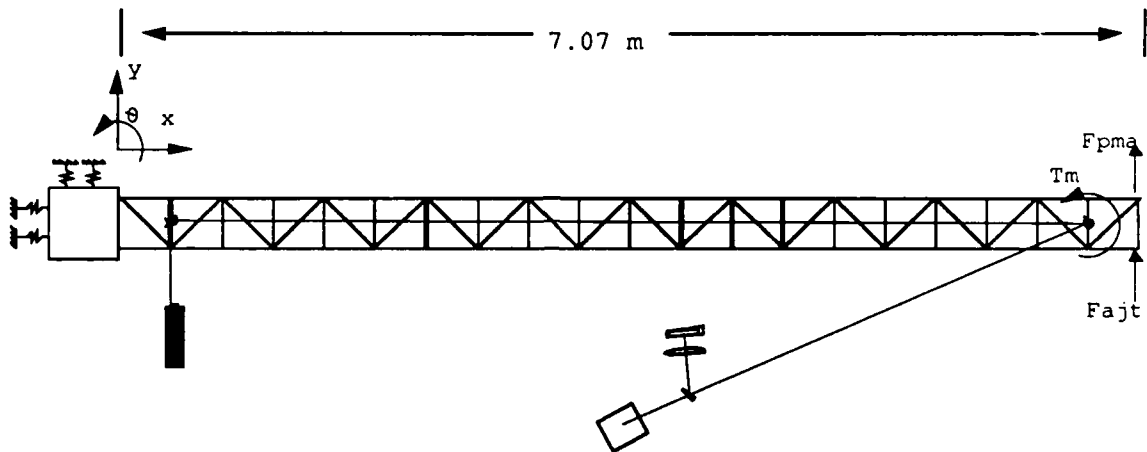


Figure 1.1: Experimental Setup

Optical disturbances are created through the base mirror. This mirror is driven to create a known beam angle disturbance profile of which the controller has no information other than a resulting position error at the sensor output. Structural disturbance of the beam path is created by exciting the truss using either air jet thrusters (AJT's) or a proof mass actuator (PMA). The tip mirror acts as the control actuator and works to reject both structural and non-structural disturbances. Both the tip and base mirrors are driven by piezo actuators which give them fast response but low angular authority. The linear photodetector acts as both a feedback signal source and as the primary measure of system performance. It does an excellent job of detecting the slightest beam motions and has outstanding high frequency response. The cylindrical lens focuses the beam in the vertical plane, thus removing any out-of-plane motion and keeping the beam in the photodetector's range. Another important sensor is a servo accelerometer, mounted at the tip, which is used in a feedforward loop. All control laws are implemented on analog computers that allow for quick changes in control settings and structure. A personal computer and a four input, one output Fourier analyzer provide data acquisition and analysis capability. Figure 1.2 shows the arrangement of experimental hardware.

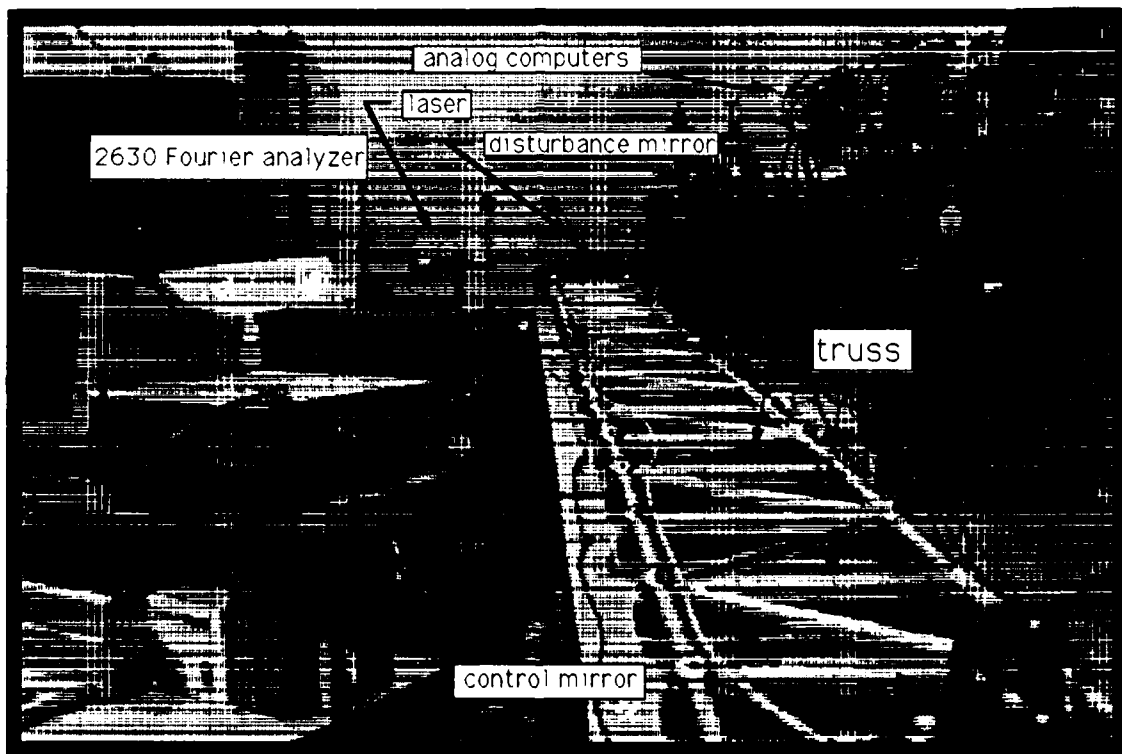


Figure 1.2: Arrangement of Experimental Hardware

### *1.3 Hardware Description*

#### *1.3.1 Truss*

The flexible planar truss structure is 7.07 meters long. It contains 20 square bays, 0.354 meters on a side and 0.500 meters on the diagonal. Steel ball bearings support the truss and allow planar motion with very little friction. The primary structural components of the 239 lb platform include aluminum truss members, hollow steel joints, and chordwise steel bars. The aluminum members and steel joints are standard modular components manufactured by Mero Corporation. The root of the truss is fixed to a heavy steel table that is bolted to the concrete floor. The first four dominant transverse natural frequencies are 1.56, 10.0, 24.7, and 43.0 Hz [Hallauer 89].

#### *1.3.2 Laser*

A 5.0 mW Helium-Neon class IIIb laser built by Uniphase Corporation is used as the beam source. The beam diameter is 0.83 mm at the origin with 1.0 mrad divergence, thus at the photodetector the beam diameter is 12 mm. The unit emits a red light of 632.8 nm wavelength and random polarization.

#### *1.3.3 Optics*

Optics used in the experiment include two mirrors, a beam splitter, and a planar-convex cylindrical lens. The mirrors are Newport Corporation model 20D10's, 3 inch in diameter with DM.4 HeNe coating. The beam splitter, a stock item from CVI Corp. is 2 inches in diameter, HeNe coated, and has 50% polarization. CVI also manufactured the cylindrical lens which is a special order item. The lens, which is HeNe coated, is  $3 \times 1.5$  inches with a 3 inch focal length.

#### *1.3.4 Piezo Actuators/Mirror Mounts*

The piezo actuated mirror, shown in Figure 1.3, is the most critical component of the experiment because it serves as the plant in the control problem formulation. The unit consists of a mirror mount, a 3 inch mirror, and a piezo translator. The

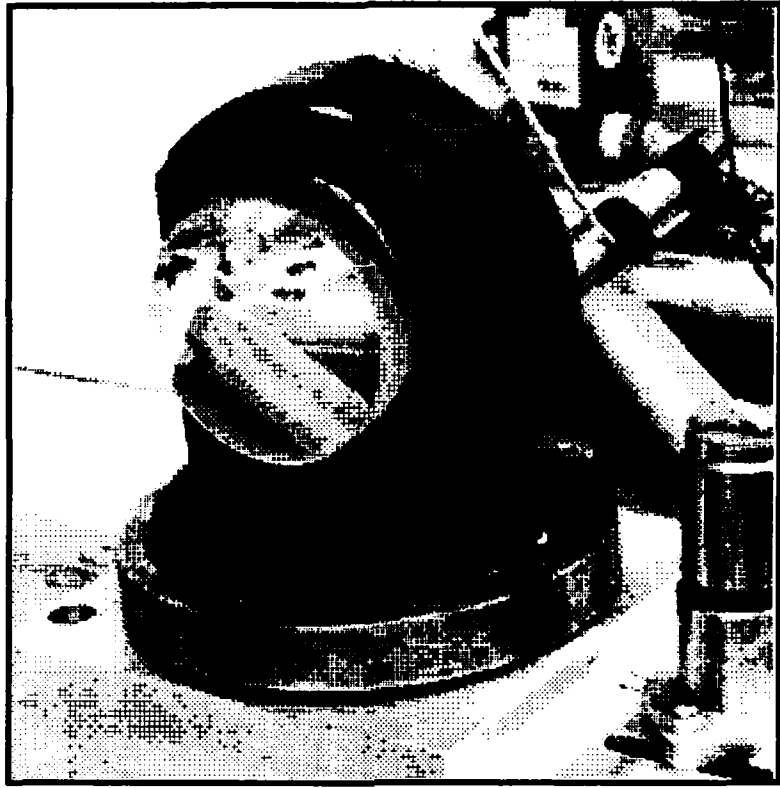


Figure 1.3: Mirror-Piezo Plant

mount, a Klinger SL 31.5, is micrometer adjustable for 50 mrad in two rotational axis. Its rotating front plate is secured by four springs. The piezo translator replaces the horizontal degree of freedom micrometer, allowing electronic control of the mirror in the x-axis. The actuator is a Polytec Optronics P-840.60 with a  $90 \mu m$  maximum expansion, 800 N maximum pushing force, and 80 N maximum pulling force. Mounting is done so that the translator provides the pushing force while the springs in the mirror mount provide the return force. The piezo stack is driven by a P-863.00 Piezo Driver-Amplifier which allows the translator to be controlled using a  $\pm 5$  volt external signal. The maximum peak-to-peak angular motion of the piezo actuated mirror is 2.5 mrad, which is enough to accommodate any structural disturbances of interest.

### 1.3.5 Photodetectors

Laser motion is monitored by a PIN-SL-76-1 optical single-axis position sensing element manufactured by United Detector Technology (UDT). The device provides a continuous signal which is linear and accurate to 99.9 % over 90 % of its working area. Its effective sensing area is  $76 \times 2.5$  mm. Responsivity is 0.6 amps/watt, position detection error is typically  $76 \mu\text{m}$ , rise time (10-90%) is typically  $30 \mu\text{s}$ , and noise current for the photodetector is  $0.4 \text{ pA}/\text{Hz}^{1/2}$ . The device is used in conjunction with a Model 301 Div signal conditioning amplifier, also made by UDT. This unit interfaces with the sensor to provide 0-10 volt position and sum outputs. The sum output is a measure of sensor illumination.

Figure 1.4 shows the power spectrum of the sensor position output under static conditions. Notice the strong noise signals with peaks at  $120 + 60 \times N$  Hz, N being an

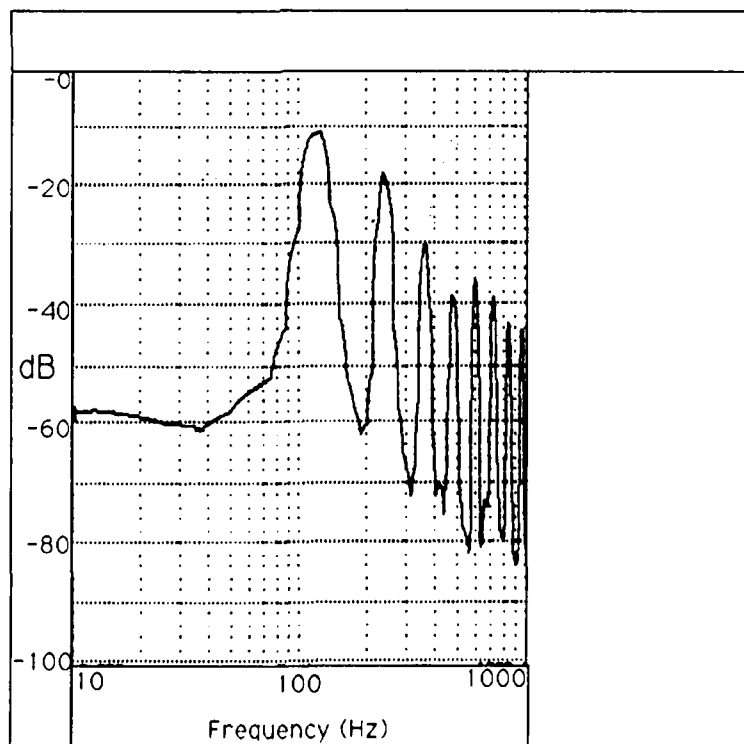


Figure 1.4: Power Spectrum of Sensor Noise

integer value  $\geq zero$ . The source of this noise is jitter in the room fluorescent lighting. To deal with this problem a black cardboard box, 12"  $\times$  5"  $\times$  5", was constructed to surround the optics-sensor setup. Two holes provide for beam entrance and exit, so a small amount of room lighting noise still exists. Figure 1.5 shows the power spectrum of the sensor output after the addition of the *black box*. The position signal noise

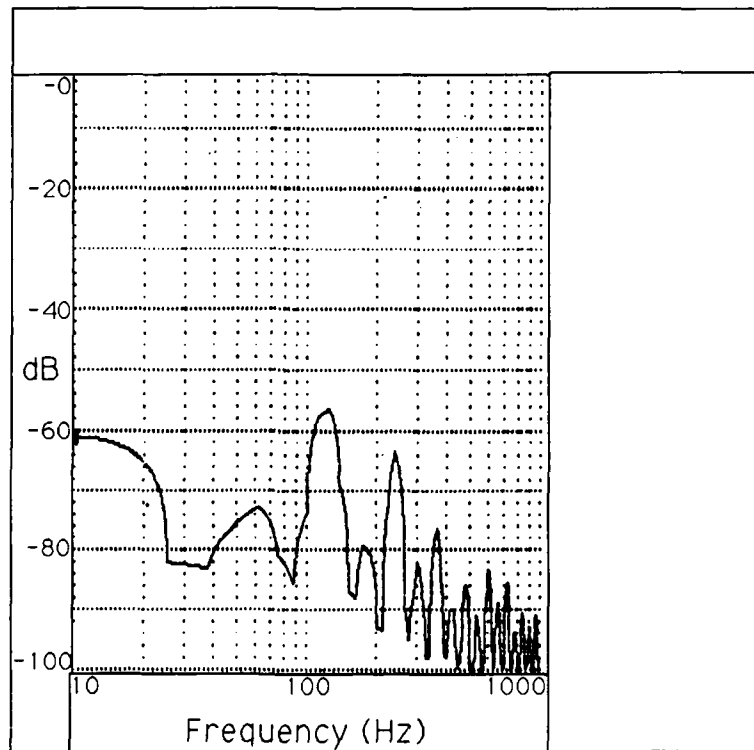


Figure 1.5: Power Spectrum of Sensor Noise with *Black Box*

is reduced from a value of 0.4182 volts rms to .002558 volts rms, a change of 46 db. The noise is still not negligible and is an important factor in the controller design.

### 1.3.6 Accelerometer

The excitation of flexible structural modes is monitored by two accelerometers mounted at the mid and tip stations of the truss. These are Sundstrand Data Control Model QA-700 servo units. The sensing resistors are set to produce 38.8 volts/g so high motion sensitivity can be achieved [Hallauer 89].

### 1.3.7 Proof Mass Actuators/Air Jet Thrusters

In order to effectively monitor disturbance rejection, some controlled way of exciting the truss is necessary. This is done primary using a tip mounted proof-mass-actuator (PMA), and to a limited extent, two tip mounted air-jet-thrusters (AJT's). The actuated mass of the PMA is a 1.4 kg alnico magnet driven by an electromagnetic coil. Feedback from a linear velocity transducer and an eddy current sensing position transducer provide position stability and damping to the PMA. The AJT's are driven by on-off triggered circuits and are powered by 60 psi lab air pressure. The tip mounted actuation hardware is shown in Figure 1.6.

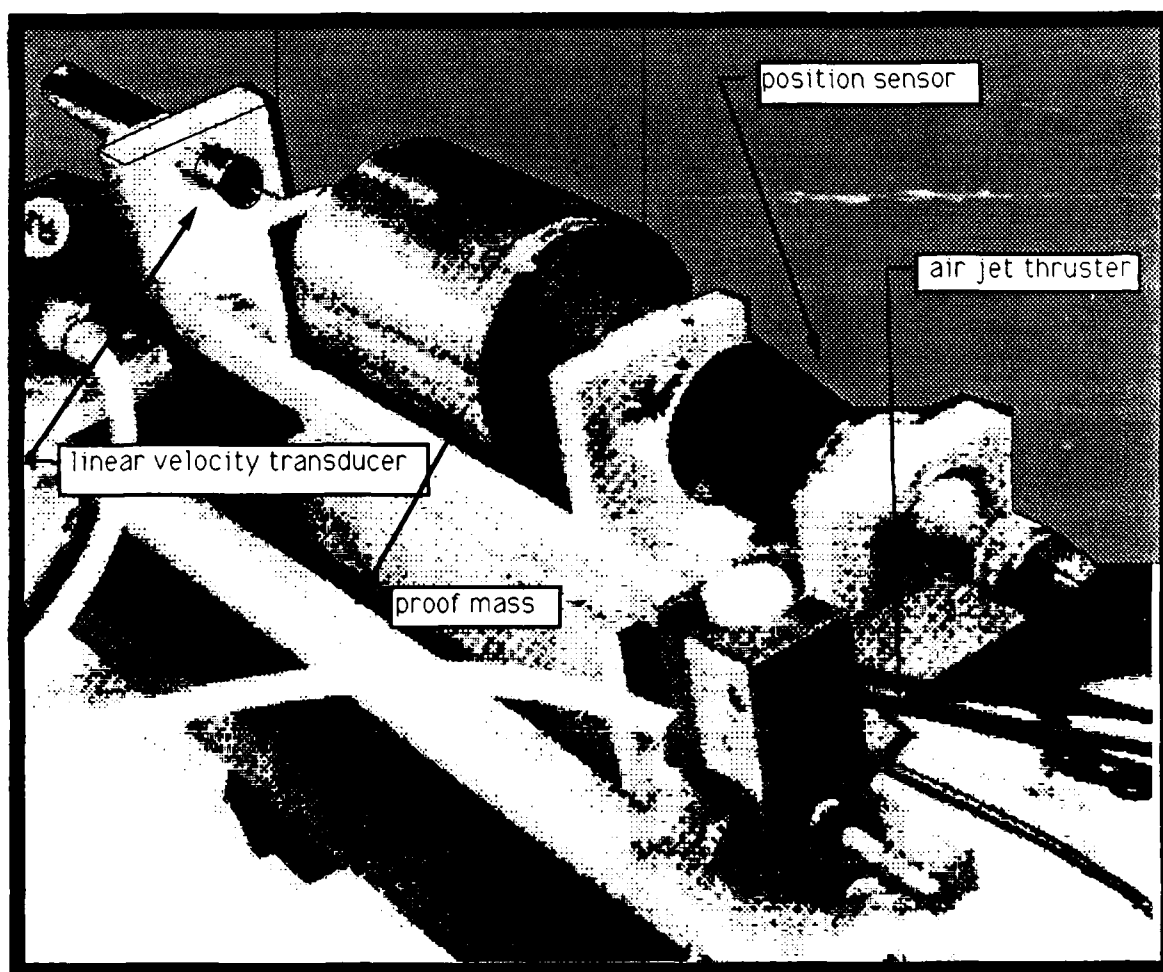


Figure 1.6: Tip Mounted Proof Mass Actuator and Air Jet Thrusters

### 1.3.8 Analog Computers

Implementation of control laws in this experiment is done almost entirely using the Comdyna GP-6 analog computer. Using banana-plug leads and adjustable pots, circuits are built quickly on the eight available operation amplifiers and potentiometers. Operating voltage is  $\pm 10$  volts. These units can be linked together when a greater number of op amps are required.

### 1.3.9 Fourier Analyzer

Data acquisition and analysis is carried out using the Tektronix 2630 Fourier Analyzer and a Zenith 248 AT personal computer. The 2630 has four analog inputs and one analog output channel. The unit has extensive time and frequency domain capabilities and comes with built in anti-aliasing filters for acquisition. The sampling rate is automatically set at 2.56 times the bandwidth of the anti-aliasing filters. It has internal computing capability to quickly perform complex operations, the primary one being the fast Fourier transform (FFT). Figure 1.7 shows the 2630 with the Zenith PC set up for data acquisition.

Using the FFT, the 2630 can derive a number of useful functions. Using two time histories  $x(i)$  and  $y(i)$  ( $i = 0,1,2,\dots,N-1$ ) one can define their transforms  $X(k)$  and  $Y(k)$  ( $k = 0,1,2,\dots,N/2$ ). Power spectrum,  $S_{xx}(k)$ , and cross-spectrum,  $S_{xy}(k)$ , are then derived.

$$S_{xx}(k) = \left(\frac{1}{P}\right) X^*(k)X(k) = \left(\frac{1}{P}\right) |X(k)|^2 \quad (1.1)$$

$$S_{xy}(k) = \left(\frac{1}{P}\right) X^*(k)Y(k) \quad (1.2)$$

$P$  is the frame time and  $*$  is complex conjugate. The statistical accuracy of the power spectrum is  $e = 1/\sqrt{M}$ , with  $M$  being the number of data blocks used in averaging the results. Once determined, the power spectrum and cross-spectrum can be used to derive a number of other functions. These include the transfer function:

$$H_{xy}(k) = \frac{S_{xy}(k)}{S_{xx}(k)} \quad (1.3)$$

the impulse response function:

$$h_{xy}(i) = FFT^{-1}\{H_{xy}(k)\} \quad (1.4)$$



Figure 1.7: Tek 2630 Fourier Analyzer and Zenith 248 AT Data Acquisition Setup

the auto-correlation function:

$$sxx(i) = FFT^{-1}[Sxx(k)] \quad (1.5)$$

and the cross-correlation function:

$$sxy = FFT^{-1}[Sxy(k)]. \quad (1.6)$$

Another useful function of the 2630 is swept sine measurements. This is done using the SWSINE.EXE program. The analog output channel generates a sine wave and automatically sweeps through a desired set of frequencies while the input channels acquire data. Magnitude and phase information is then derived and stored. The SWSINE function is very useful in cases where a noisy input signal is not suitable or when output data is heavily corrupted with noise [Tektronix 89].

## Chapter 2

### MODELING AND CONTROL THEORY

#### 2.1 Actuated Mirror Modeling

##### 2.1.1 Model Structure

The first step in modeling the mirror-piezo unit, shown in Figure 2.1, is to analyze its physical properties and define basic relationships. The piezo translator has

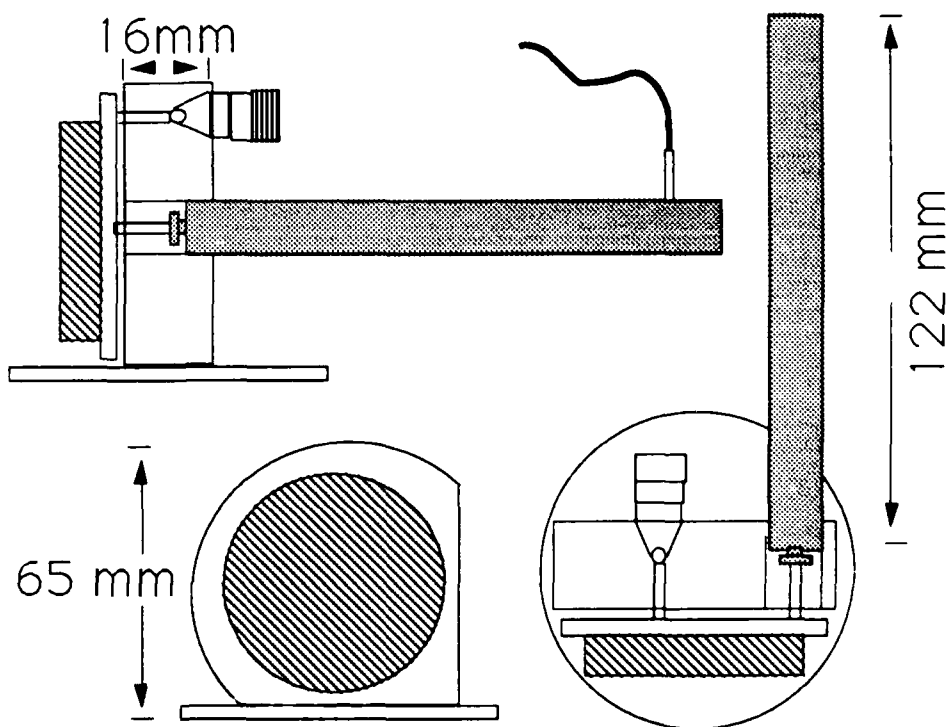


Figure 2.1: Mirror-Piezo Layout

a mechanical resonance of 6 kHz, well beyond the range of interest in this experiment. The transfer function from piezo voltage input to translator position output,  $X_{piezo}(s)/V_{piezo}(s)$ , can be treated as a DC gain. The piezo driver-amp is also

high bandwidth so the transfer function from amplifier control voltage input to amplifier output,  $V_{piezo}(s)/V_{control}(s)$ , is treated as a gain of 10. The translator has a nominal expansion of 90 micrometers at 100 volts and the moment arm from the piezo to the pivot point is approximately 40 mm. This gives an initial estimate of  $2.25\text{mrad}/100\text{volts}$  for the static value of  $\Theta_{mirror}(s)/V_{piezo}(s)$ , the transfer function from piezo voltage input to mirror angle output. The dynamic behavior in the plant comes from the mirror mount and four springs that secure the face plate. There is no physical component of the mount that adds damping besides friction. The transfer function from the amplifier control voltage input to mirror angle output for the mirror-piezo plant is therefore assumed to be that of a second order spring-mass-damper system with low damping.

$$\frac{\Theta_{mirror}(s)}{V_{control}(s)} = \frac{K_m \omega_m^2}{s^2 + 2\xi_m \omega_m s + \omega_m^2} \quad (2.1)$$

An optical gain is present in the system due to the fact that the angle of incidence equals angle of reflection.

$$\Theta_{beam} = 180^\circ - \Theta_{incidence} - \Theta_{reflection} = 180^\circ - 2 \times \Theta_{incidence} \quad (2.2)$$

As the  $\Theta_{incidence}$  changes by  $\Delta$ , the beam angle changes by  $2 \times \Delta$ , so there is a gain of 2 between the mirror angle and the beam angle.

### 2.1.2 Experimental Development

Experimental analysis of the mirror-piezo transfer function is performed using the transfer function mode of the 2630 Fourier analyzer. A 0.50 volt rms white noise signal is sent into the piezo driver while the corresponding beam motion is monitored by the linear photodetector. The computer uses the input and output sequences along with the FFT to generate magnitude and phase information. The results from ten frames of 1024 data points are averaged to provide information from 0 to 5000 Hz. The anti-aliasing filters are set at 5 kHz and the sampling rate is 12.8 kHz.

The results in Figure 2.2 show the experimental transfer function (solid line) and the theoretical model (dashed line) with the parameters  $K_m = 0.25$ ,  $\omega_m = 500 \times (2\pi)$  rad/s, and  $\xi_m = 0.10$ . It is seen that the model matches the experimental

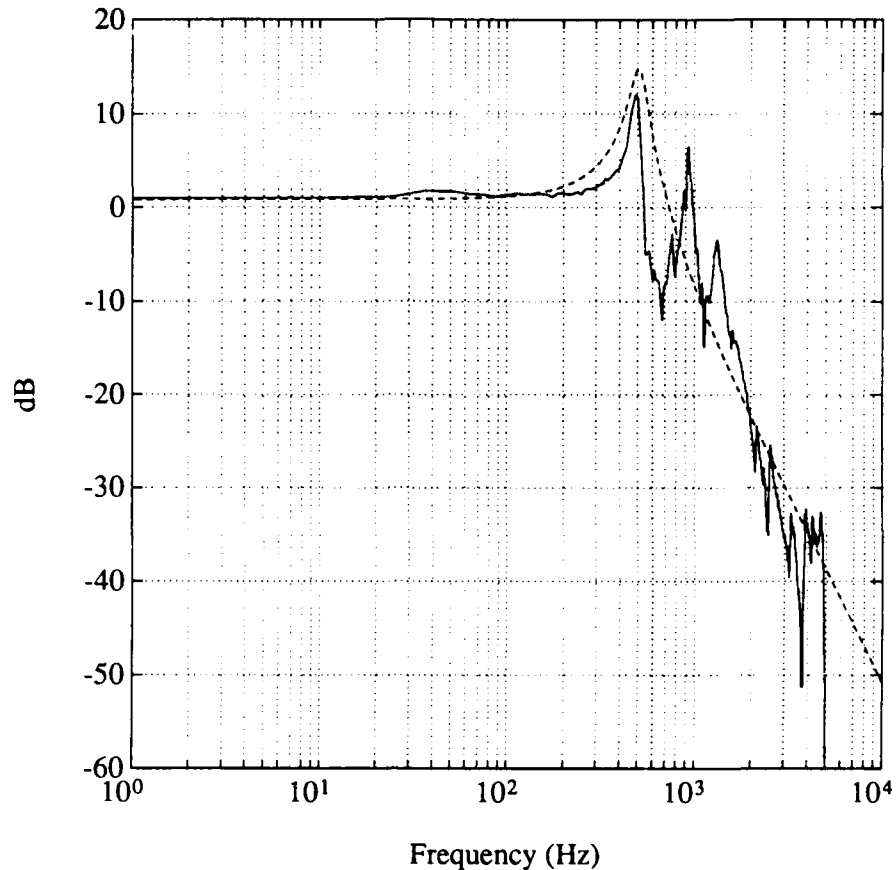


Figure 2.2: Experimental and Theoretical Mirror-Piezo  $V_{sens}/V_{control}$

results quite closely. Damping is low, as can be seen by the high peaking at the resonance frequency. A number of lesser peaks exist after the resonance peak. These harmonics of the natural frequency show up at integer multiples of 500 Hz and exist as a result of the experimental nature of the analyzed data. The natural frequency of the plant is at 500 Hz, very high with respect to the modes of the truss that generate the structural disturbances. This is good news because the mirror-piezo unit acts like a DC gain at those frequencies and avoids potential structural interaction problems.

## 2.2 Controller Design

### 2.2.1 Closed Loop Design

The primary objective of this design is the rejection of structural and optical disturbances. An important closed loop measure of performance in a pointing system is bandwidth, and so command following must be considered. The rejection of high frequency sensor noise is also critical in a realizable design. Figure 2.3 is a simple

unity feedback block diagram that shows how reference inputs -  $R(s)$ , disturbances -  $D(s)$ , and noise -  $N(s)$  enter the closed loop system.  $G(s)$  is the plant and  $K(s)$  the controller.

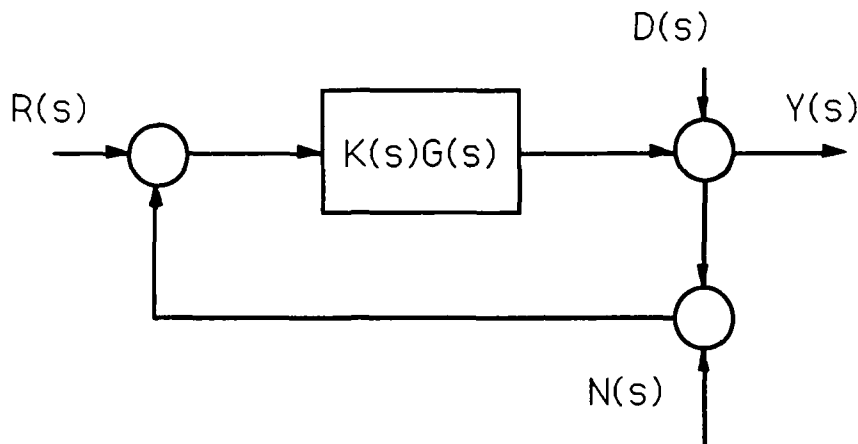


Figure 2.3: Unity Feedback Block Diagram

The goal of disturbance rejection is to have the relationship :

$$\frac{Y(s)}{D(s)} = 0 \quad \text{for} \quad \omega < \omega_{\text{bandwidth}}$$

The plant disturbance transfer function is

$$\frac{Y(s)}{D(s)} = \frac{1}{1 + K(s)G(s)}$$

so we want

$$K(s)G(s) \Rightarrow \infty \quad \text{for} \quad \omega < \omega_{\text{bandwidth}}$$

The goal of command following is to have the relationship :

$$\frac{Y(s)}{R(s)} = 1 \quad \text{for} \quad \omega < \omega_{\text{bandwidth}}$$

The command transfer function is

$$\frac{Y(s)}{R(s)} = \frac{K(s)G(s)}{1 + K(s)G(s)}$$

so again we want

$$K(s)G(s) \Rightarrow \infty \quad \text{for} \quad \omega < \omega_{\text{bandwidth}}.$$

Noise rejection is achieved through the relationship :

$$\frac{Y(s)}{N(s)} = 0 \quad \text{for} \quad \omega > \omega_{\text{bandwidth}}.$$

The signal noise transfer function

$$\frac{Y(s)}{N(s)} = \frac{K(s)G(s)}{1 + K(s)G(s)}$$

so we want

$$K(s)G(s) \Rightarrow 0 \quad \text{for} \quad \omega > \omega_{\text{bandwidth}}.$$

The only variable parameters in these equations are those in  $K(s)$ , the controller. The relationships dictate that the controller have high gains at low frequencies to achieve disturbance rejection and command following, and low gains at high frequencies for noise rejection. The frequency,  $\omega_{\text{bandwidth}}$ , is driven by the performance requirements and noise characteristics of the experiment. The highest of the first four dominant transverse structural modes, 40 Hz, drives the low end for  $\omega_{\text{bandwidth}}$ . The noise spectrum of the sensors limits the high end values of  $\omega_{\text{bandwidth}}$ . A simple classical technique for achieving the desired gain profile is the use of proportional-integral (PI) feedback,  $K(s) = K_p(s + \frac{K_i}{K_p})/s$ . The integral action in the PI controller guarantees zero steady-state error, an important quality in pointing systems. The proportional- $K_p$  and integral- $K_i$  gains are chosen to satisfy the disturbance rejection, bandwidth, and noise rejection requirements. Stability must also be maintained, increasing  $K_p$  pushes the closed loop poles of the system towards the right half of the s-plane. Hardware issues such as voltage limitations and actuator saturation also restrict the magnitude of gains.

### 2.2.2 Feedforward Design

There are different types of disturbances on a system. These can be classified into two groups: those which can be observed, and those which are unobservable. When some

part of a disturbance can be measured, it may be used in conjunction with an open loop, feedforward path to provide rejection. This idea is illustrated in Figure 2.4.  $D1(s)$  is the part of the disturbance that can be measured. The transfer function from the observable disturbance input to the output is

$$\frac{Y(s)}{D1(s)} = \frac{1 + F(s)G(s)}{1 + K(s)G(s)} \quad (2.3)$$

If  $F(s) = -G(s)^{-1}$ ,  $Y(s)/D1(s)$  will equal zero, and perfect disturbance rejection will be achieved for  $D1(s)$ . In reality it is impossible to exactly invert a system.

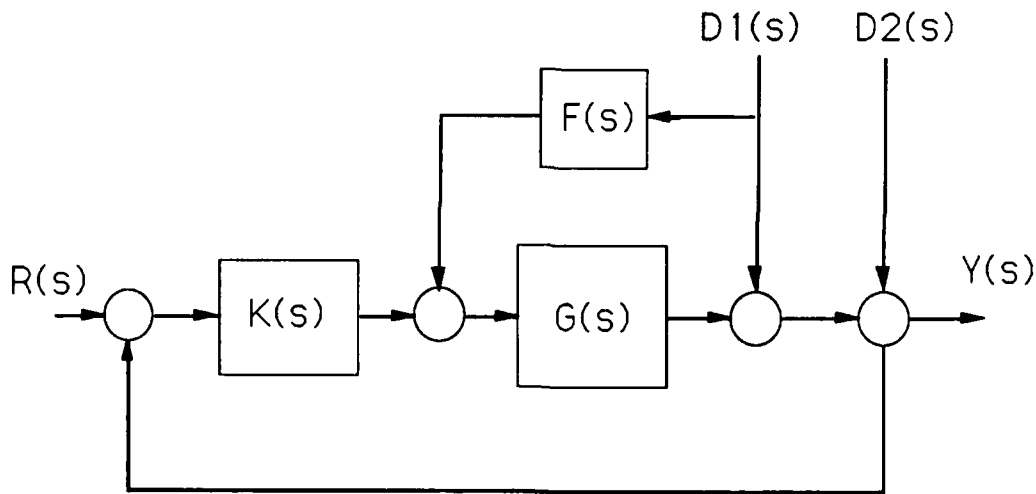


Figure 2.4: Feedforward Control Block Diagram

Even in the single-input/single-output case the linear model  $G(s)$  is never exact. Physical systems are almost always strictly proper, so their inverses are normally not realizable. Despite these problems, some benefit can still be derived from the information about the observable disturbance. A feedforward compensator uses the available information to mitigate the effects of the approximately linear disturbance.

In the case of the disturbance rejection problem, the plant transfer function,  $G(s) = \Theta_{mirror}(s)/V_{control}(s)$  (see equation 2.1), is strictly proper. Its inverse

$$G(s)^{-1} = \frac{1}{K_m \omega_m^2} s^2 + \frac{2\xi_m}{K_m \omega_m} s + \frac{1}{K_m} \quad (2.4)$$

is not normally realizable as it contains differentiation and double-differentiation terms. Note that in the time domain the feedforward output is

$$V_{feedforward}(t) = -\frac{1}{K_m \omega_m^2} \ddot{\Theta}_{dist}(t) - \frac{2\xi_m}{K_m \omega_m} \dot{\Theta}_{dist}(t) - \frac{1}{K_m} \Theta_{dist}(t). \quad (2.5)$$

The unobservable part of the disturbance is beam jitter and target vibration. The observable disturbance is the beam motion induced through the excitation of flexible structural modes in the planar truss. This motion can be sensed through the accelerometer mounted at the tip station of the truss. The accelerometer is aligned in the Y-axis to detect transverse acceleration (see Figure 1.1 on page 2). Assuming that the dominant source of structure induced disturbance on the beam path is transverse motion, a  $\ddot{\Theta}_{dist}(t)$  can be derived from the accelerometer output. This term can be integrated to approximate  $\dot{\Theta}_{dist}(t)$  and again to find  $\Theta_{dist}(t)$ . These estimates of the disturbance states may be multiplied by the gains in equation 2.5 to implement a feedforward controller that approximates the inverse of the plant.

## Chapter 3

### EXPERIMENTAL RESULTS

#### 3.1 Design Limitations

The physical limitations of the experimental problem are the driving forces behind the final selection of a controller. Achieving high bandwidth and rejection over a broad frequency range drives the integral gain to large values. The 20 db/decade roll-off of  $K(s)$  up to  $(K_i/K_p)/2\pi$  Hz along with the 40 db/decade roll-off of  $G(s)$  at 500 Hz gives the combined open loop forward transfer function  $K(s)G(s)$  the desired gain profile as discussed in section 2.2.1. The bandwidth of the closed loop system and thus the zero db crossover frequency is limited by the noise characteristics of the system. The room lighting jitter discussed in section 1.3.5 is the major source of noise affecting the design. The bandwidth of the system should be kept below 120 Hz so that noise rejection will occur at the critical frequencies. The high frequency noise problems along with stability requirements also limit the value of  $K_p$ . Increasing the proportional gain has the affect of both increasing the gains at high frequencies and pushing the characteristic roots toward the right half of the s-plane. Noise considerations also prohibited the addition of stabilizing derivative or lead compensation into the design. These were attempted and unavoidably created unacceptable noise amplification.

Another constraint on the magnitude of  $K(s)G(s)$  is power and speed limitations of the control and actuation hardware. When the amplified error signal grows faster than the piezo-actuated mirror can react, the GP-6's operational region of  $\pm 10$  volts is exceeded and its circuitry overloads. This limitation is due to the current limited expansion time of the piezo. The shortest expansion time for the translator is governed by the equation

$$t_{expansion} = \frac{i_{max}}{2 \times C \times V_0} \quad (3.1)$$

$C$  is the electric capacitance of the piezo stack -  $10.8\mu F$ ,  $i_{max}$  is the amplifier maximum average current output - 60 mA, and  $V_0$  is the input voltage. As gains are increased,

the values of  $V_0$  the piezo amp sees grow linearly. The compensator gain is thus limited by the current capabilities of the piezo amplifier and the capacitive properties of the piezoelectric translator that drives the mirror.

### 3.2 Final Controller Selection

The overall structure of the controller with PI feedback and feedforward compensation is shown in Figure 3.1.

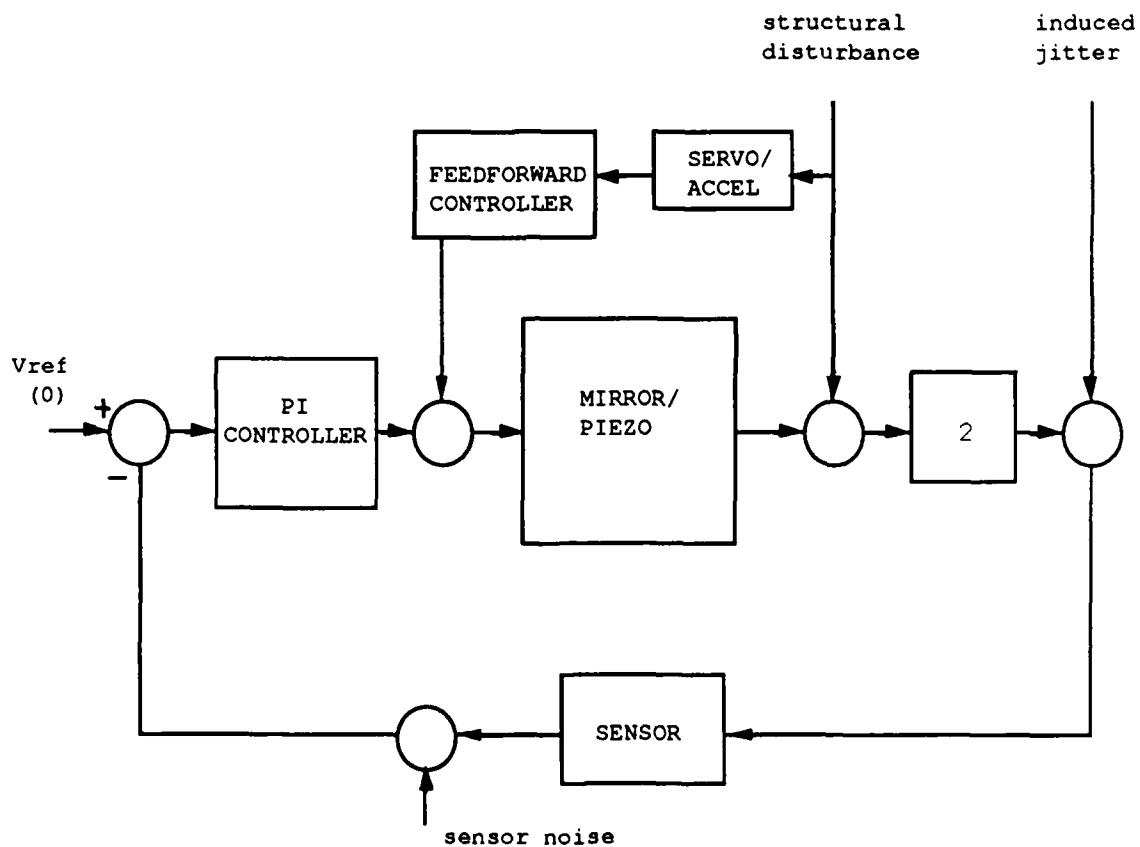


Figure 3.1: Block Diagram of Overall Control Structure

#### 3.2.1 PI Controller

The final compensator selection is made taking into consideration all of the theoretical design issues and actual hardware constraints. PI feedback is the chosen control

structure for the reasons of simplicity and ease of implementation. Tuning of gains is done through a trial and error approach, pushing for maximum disturbance rejection, while limited by stability, noise, and control saturation considerations. The result is a compensator of the form

$$G_c(s) = \frac{0.5(s + 1000)}{s}. \quad (3.2)$$

The gain profile of the PI controller has the desirable characteristics discussed in section 2.2.1. A magnitude plot of  $K(s)$  is shown in Figure 3.2. The resulting open

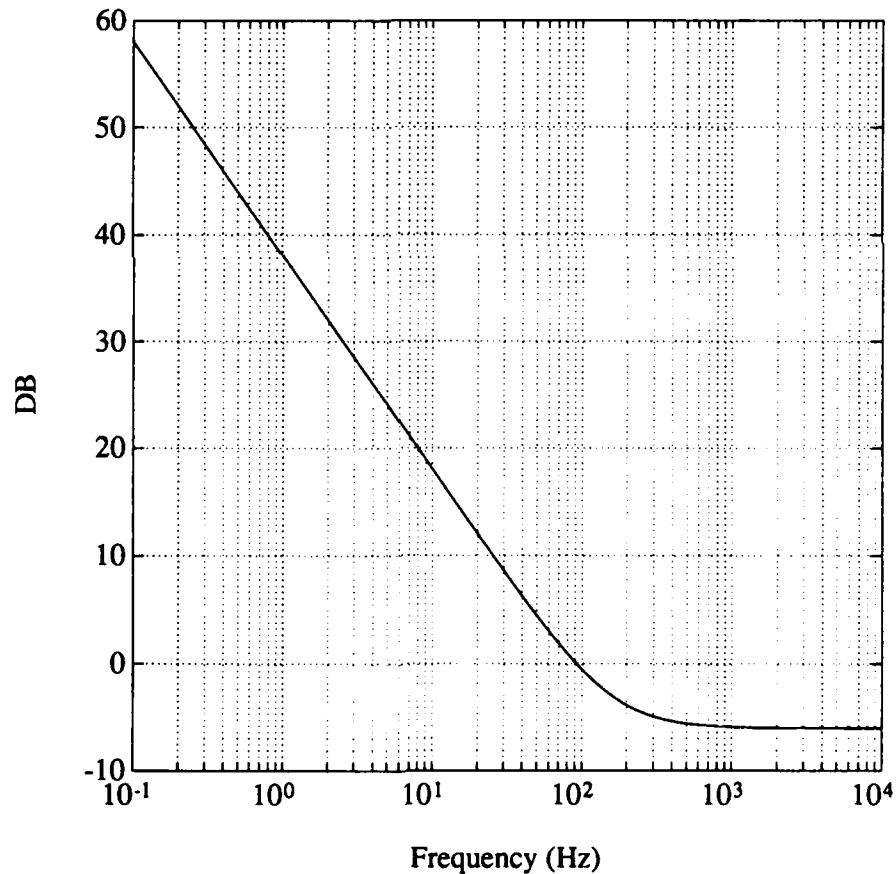


Figure 3.2: Magnitude Plot of PI Controller,  $K(s)$

loop forward transfer function has high gains at low frequencies and low gains at high frequencies. The magnitude plot of  $K(s)G(s)$  is shown in Figure 3.3.

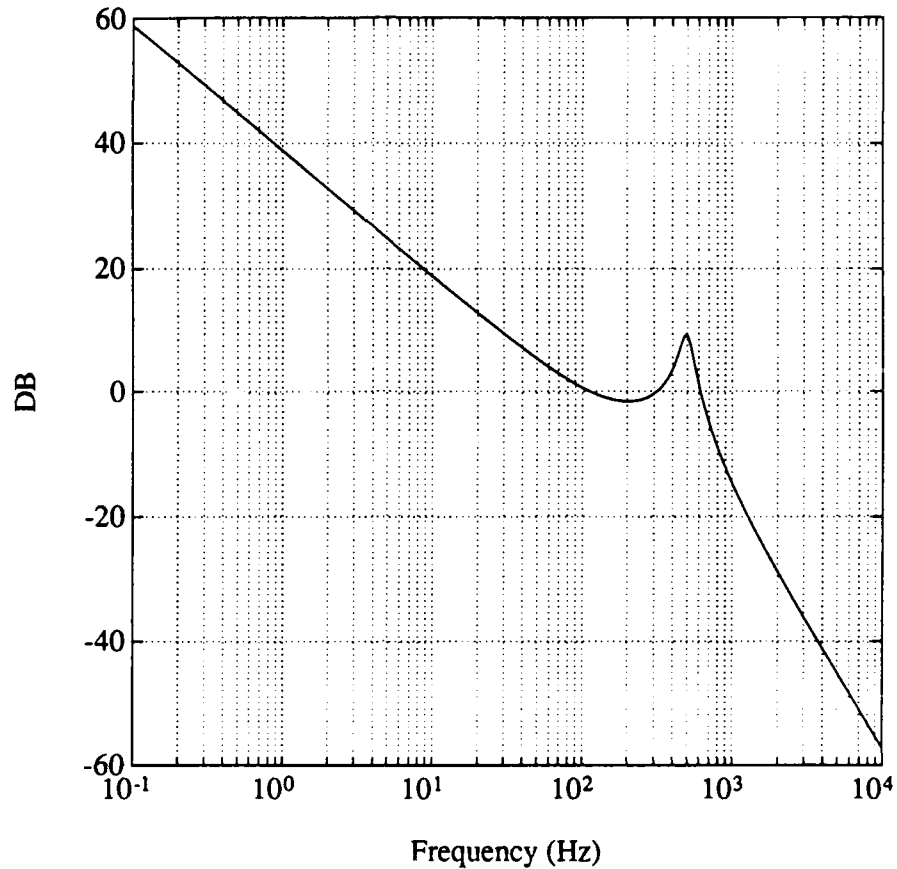


Figure 3.3: Magnitude Plot of the Forward Transfer Function  $K(s)G(s)$

The implemented design is stable with 6.4 db gain margin in the proportional loop and 2.5 db gain margin in the integral loop. This means  $K_p$  can be increased by a factor of 2.1 before instability occurs, but noise becomes a problem before stability.  $K_i$  can be increase by a factor of 1.33 before instability occurs. The integral gain is pushed to the limit to get the maximum possible disturbance rejection. The analog computer implemented circuit is shown in Figure 3.4.

### 3.2.2 Feedforward Controller

Implementing the feedforward loop requires a pseudo plant inversion as described in section 2.2.2. When the mirror-piezo plant parameters are put into equation 2.5, the resulting control law is

$$V_{feedforward}(t) = -4.05 \times 10^{-7} \ddot{\Theta}_{dist}(t) - 5.09 \times 10^{-4} \dot{\Theta}_{dist}(t) - 4\Theta_{dist}(t). \quad (3.3)$$

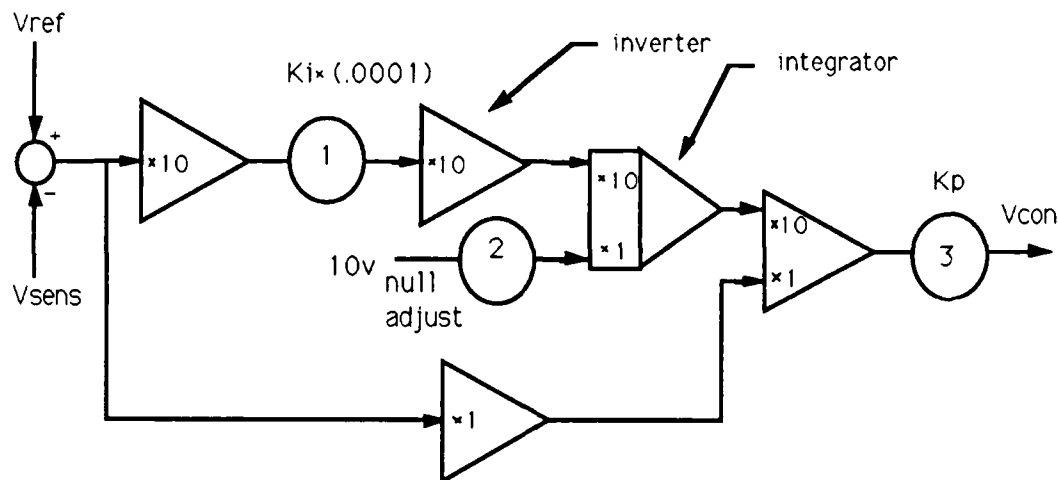


Figure 3.4: Circuit Diagram of PI Controller

Accelerometer dynamics exist at frequencies in the kHz range, far above the desired control bandwidth of the design. The accelerometer output is therefore assumed to be  $\ddot{Y}(t)_{tip} + \text{high frequency noise}$ . For small disturbance angles, the angular acceleration,  $\ddot{\Theta}_{tip \text{ disturbance}}$  is assumed to be directly proportional to the transverse acceleration  $\ddot{Y}(t)$ . This assumption is good as long as the truss behaves as an Euler-Bernoulli beam with longitudinal modes of magnitudes negligible in relation to the transverse (lateral) modes. The validity of this method for the first four modes was verified by observing the phase relationship between the photodetector signal and the accelerometer output. These are precisely  $180^\circ$  out of phase for the modes of interest.

Integration of the  $\ddot{Y}(t)_{tip}$  signal is done using approximate circuits. It is impossible to exactly integrate sensor output because any DC component of the signal, no matter how small, will grow and eventually ruin the feedback. A second order approximate integrator is used so that zero DC gain can be achieved.

$$G_{integrator}(s) = \frac{s}{s^2 + \omega_r s + \omega_r^2} \quad (3.4)$$

The value used for  $\omega_r$  is 0.628 [Hallauer 89]. Notice that when  $s = j\omega = 0$ ,  $G_{integrator}(0) = 0$ . Thus any DC signal in the accelerometer output is ignored. The GP-6 analog computer implemented circuit is shown in Figure 3.5. Two of these

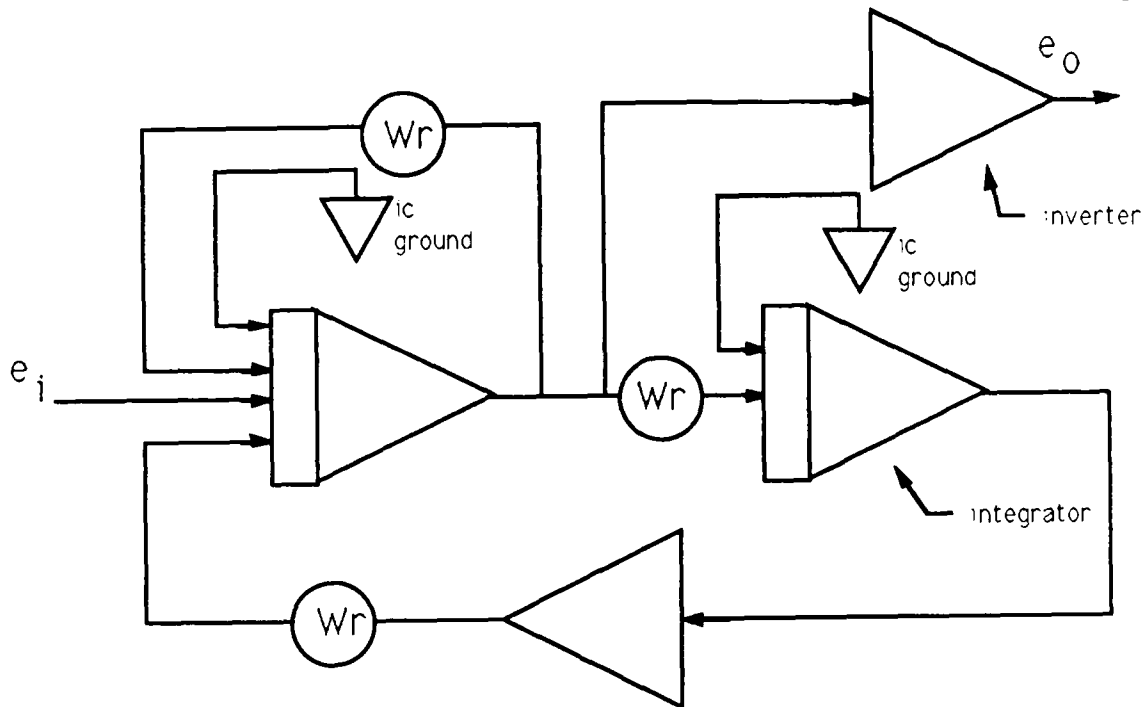


Figure 3.5: Circuit Diagram of Approximate Integrator

circuits are used in series to provide the  $\dot{\Theta}_{tipdisturbance}$  and  $\Theta_{tipdisturbance}$  signals required for feedforward implementation.

The gain values shown in equation 3.3 must be scaled and implemented using potentiometers. The  $\ddot{\Theta}_{dist}(t)$  gain is so small that the corresponding output signal never gets beyond the noise range of the circuitry. The  $\dot{\Theta}_{dist}(t)$  gain is also very small. Implementation demonstrated that this disturbance velocity path does not make a positive contribution to disturbance rejection for the modes of interest. The problem once again is poor signal-to-noise ratio for the very low voltage signals. The  $\Theta_{dist}(t)$  gain is four orders of magnitude larger than the others, the actual value is tuned by starting at the theoretical setting and adjusting until maximum rejection is achieved across the frequency spectrum. The implementation of the feedforward controller with only the disturbance angle path, the twice integrated accelerometer output multiplied by a gain, gives good low frequency open loop rejection. The omission of the velocity and acceleration loops causes a loss in the rejection benefit as frequency increases. The feedforward controller should never cause more than a slight increase in net disturbance angle, even at very high frequencies. More accurate implementation hardware would allow for a more effective pseudo-inversion of the plant that includes  $\ddot{\Theta}_{dist}(t)$  and  $\dot{\Theta}_{dist}(t)$  loops.

### 3.3 Command Following and Noise Rejection

As discussed in section 2.2.1, the command following and noise rejection properties of the system may be examined using the unity feedback form of the closed loop transfer function,  $K(s)G(s)/(1 + K(s)G(s))$ . This transfer function is evaluated experimentally by applying a reference voltage at the input and monitoring the response at the sensor output. The Tektronix 2630 Fourier analyzer is used to apply a white noise signal at  $V_{ref}$ . The input and output signals are sampled and used to derive a frequency response plot as discussed in section 1.3.9. Figure 3.6 shows the resulting experimental magnitude results. The dashed line is the theoretical evaluation of the closed loop function using the linear model. The peaking at resonance has

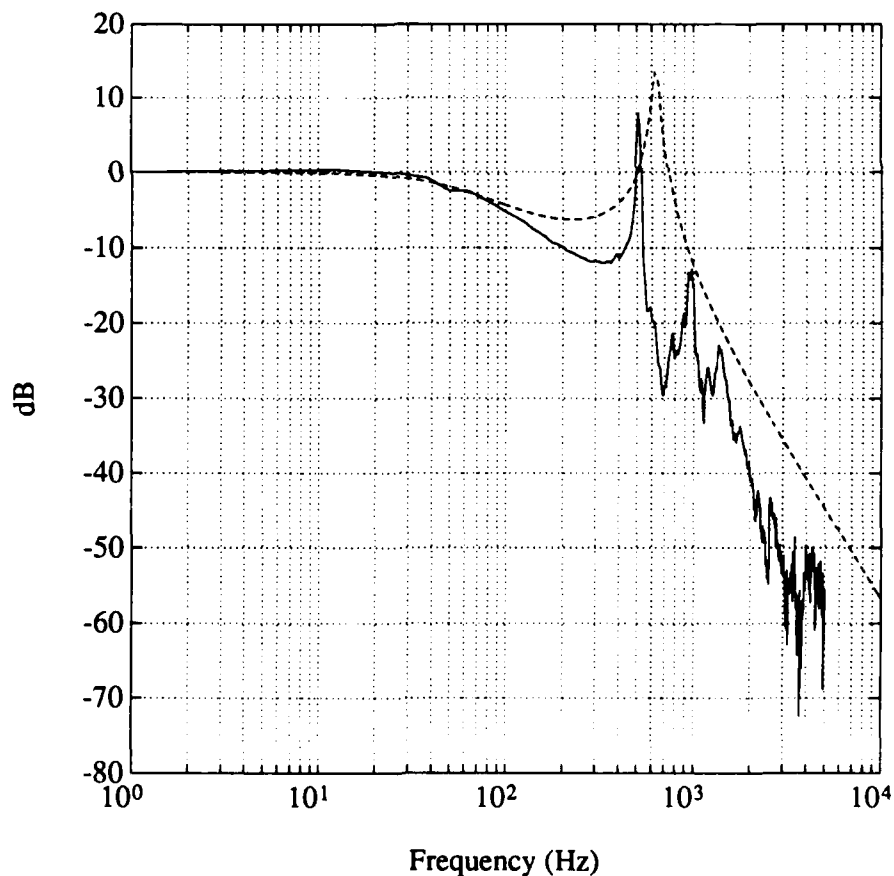


Figure 3.6: Experimental and Theoretical  $V_{sensor}/V_{reference}$  of the Closed Loop System

increased from the open loop results due to the loss of damping with the PI feedback. Figure 3.7 shows the same transfer function obtained using the sine sweep capability of the 2630. The -3 dB crossover point on both experimental plots is 60 Hz. This

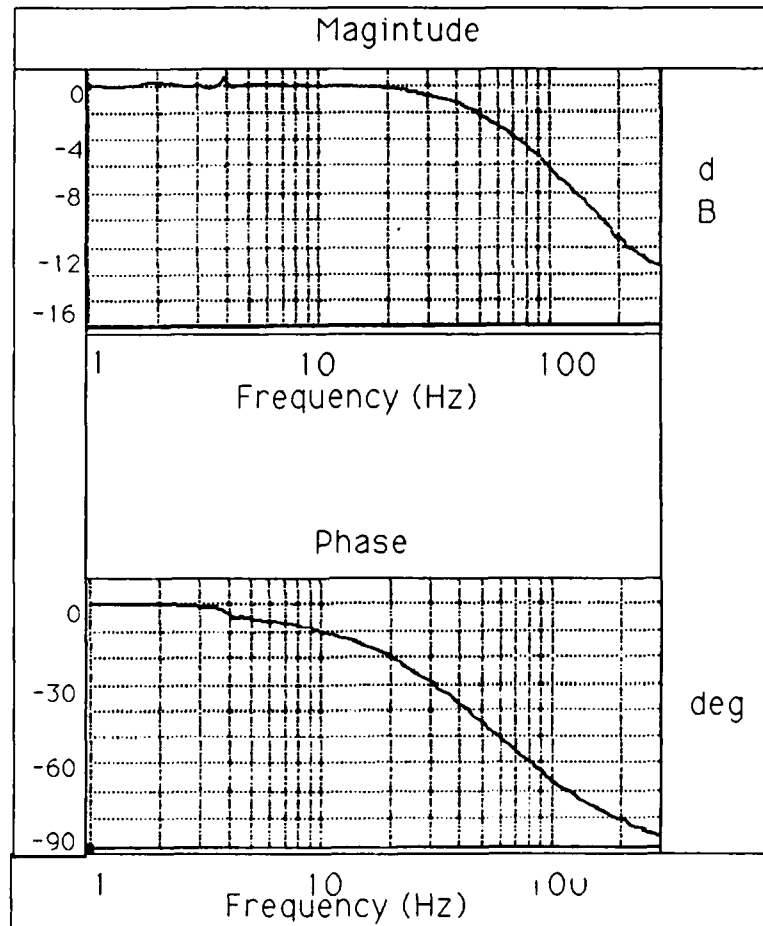


Figure 3.7: Sine Sweep of  $V_{sensor}/V_{reference}$  for Closed Loop System

closed loop bandwidth is at a higher frequency than the first four dominant transverse modes. The bandwidth is less than the dominant noise components which exist at 120 Hz and above as noted in section 1.3.5. A good trade-off has therefore been achieved between the desire for high bandwidth and noise considerations.

### 3.4 Disturbance Rejection

The rejection of line-of-sight disturbances caused by the excitation of the flexible structural modes of the planar truss is the primary design goal. The structural disturbance rejection capabilities of the system are analyzed by exciting the truss and comparing the open and closed loop beam motion. The first method used involves driving the PMA with a white noise input from the 2630 Fourier analyzer. The transfer function routine as described in section 1.3.9 is invoked to derive a magnitude plot of the input-output relationship in the frequency domain. This is done for the open loop, feedforward loop closed, PI loop closed, and for PI and feedforward loops closed cases. The results are shown in Figure 3.8. Note that the third mode barely

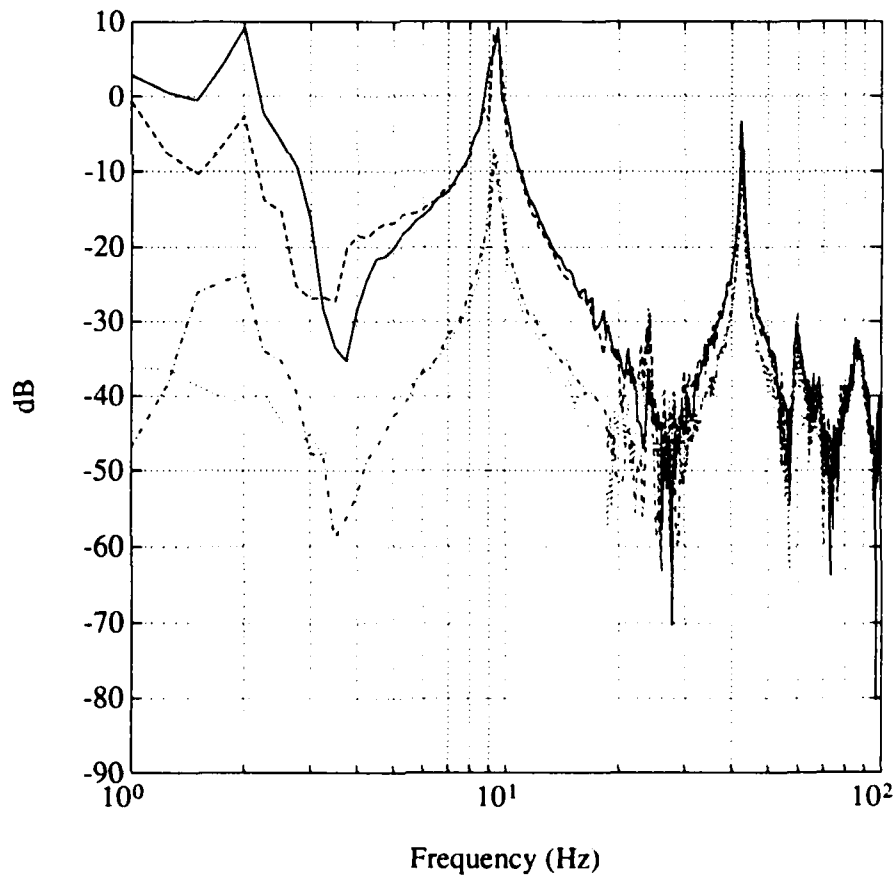


Figure 3.8:  $V_{sensor}/V_{PMA}$  for OL(-), OL FF(--), CL(-.), and CL FF(···)

shows up in the frequency responses. The control mirror is mounted one truss station in from the tip. It turns out that this position is very close to a node of the third mode and thus the 24.7 Hz motion is very lightly observable through the sensor output.

The magnitude plots in Figure 3.8 can be used to derive disturbance rejection for the system with the PI loop closed. The relevant relationships are:

$$\left( \frac{V_{beam_{CL}}}{V_{PMA}} \right) = \frac{V_{beam_{CL}}}{V_{beam_{OL}}} = \frac{K_{beam} \Theta_{beam_{CL}}}{K_{beam} \Theta_{beam_{OL}}} = \frac{\Theta_{beam_{CL}}}{\Theta_{disturbance}} \quad (3.5)$$

and

$$\begin{aligned} 20 \times \text{Log}_{10} \left( \frac{\Theta_{beam_{CL}}}{\Theta_{disturbance}} \right) &= 20 \times \text{Log}_{10}(\Theta_{beam_{CL}}) - 20 \times \text{Log}_{10}(\Theta_{disturbance}) \quad (3.6) \\ &= \frac{V_{beam_{CL}}}{V_{PMA}}(dB) - \frac{V_{beam_{OL}}}{V_{PMA}}(dB). \end{aligned}$$

Note that  $V_{beam} = V_{sensor}$ . Thus the magnitude plot of the open loop transfer function is subtracted from the magnitude plot of the closed loop transfer function to find a disturbance rejection frequency response curve.

A second method for finding line-of-sight disturbance rejection is to excite each structural mode discretely by applying a sinusoidal input through the PMA or AJT's at the natural frequency of interest. The AJT's are used to excite the first mode while the PMA is more effective for the second, third, and fourth modes. The steady state root-mean-squared output voltage is derived for the open loop, feedforward loop closed, PI loop closed, and for PI and feedforward loops closed cases for each mode. Disturbance rejection is derived through the relationship

$$\frac{\Theta(t)_{beam_{ss}}}{\Theta(t)_{disturbance_{ss}}} = \frac{\text{rms}(V(t)_{beam_{CL}})}{\text{rms}(V(t)_{beam_{OL}})} \quad (3.7)$$

The result is three discrete disturbance rejection values at each of the four modes. These values are shown in Table 3.1. The discrete points and the FFT derived frequency response curve are presented in Figure 3.9.

Table 3.1: Discrete Disturbance Rejection Values in dB

	Mode 1 1.60 Hz	Mode 2 9.50 Hz	Mode 3 24.6 Hz	Mode 4 43.3 Hz
CL	-34.3	-19.4	-11.0	-4.40
FF	-24.1	-0.44	+0.72	-0.39
CL-FF	-60.1	-20.2	-11.2	-4.67

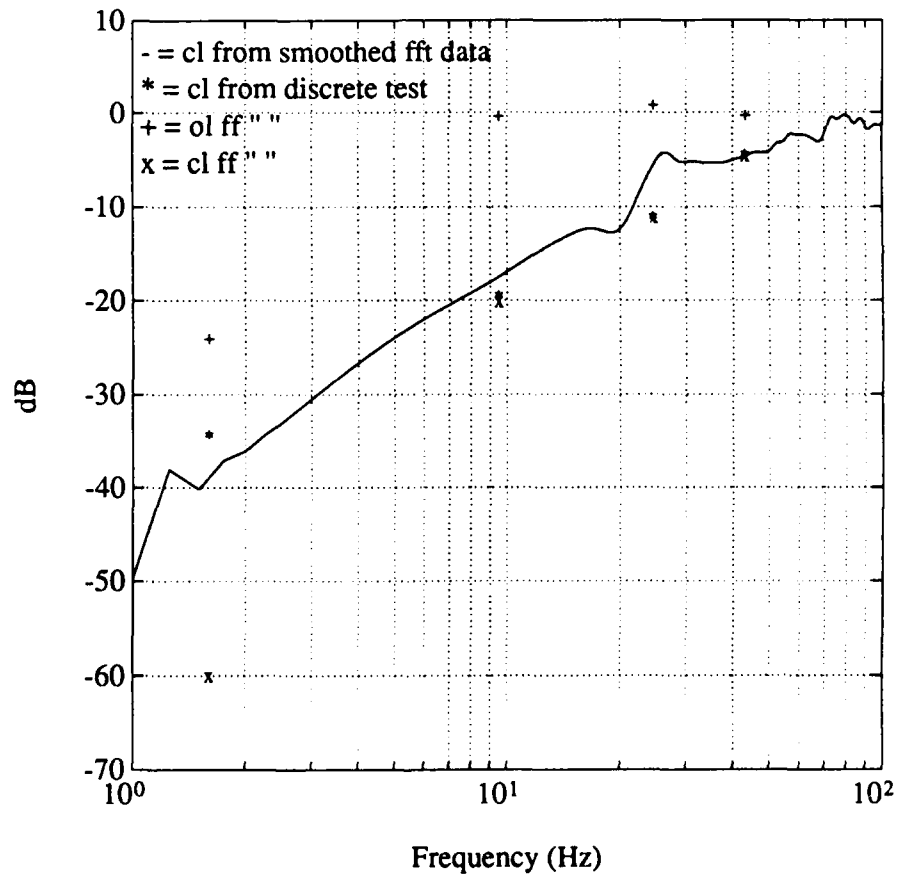


Figure 3.9: Structural Disturbance Rejection from Acquired Data

Note that the performance of the feedforward controller drops off rapidly after the first mode and actually creates a slight magnification of the disturbance at the

third mode. This limited high frequency performance is due to factors discussed in section 3.2.2. The completely implemented system with PI and feedforward loops closed demonstrates very good rejection for the first two modes. Performance at these modes is critical for satisfactory performance because they are dominant in magnitude (see Figure 3.8). Disturbance rejection is additive between the PI and feedforward loops, that is the rejection with both implemented is approximately the sum of the rejections for the single loop cases. This property is desirable because if one loop is broken for any reason, the other loop continues normal operation to provide structural disturbance rejection.

## Chapter 4

# LASER POINTING SYSTEMS

### 4.1 *Introduction*

Pointing systems as described in section 1.1 normally require a range of beam motion greater than the  $\pm 2.5$  mrad provided by the mirror-piezo assembly. Spaced based communications and astronomical systems require slow large scale angular pointing to compensate for the Earth's rotation and orbital motion. Space Defense Initiative type hardware must also deal with target trajectories. A logical extension of the disturbance rejection system discussed in chapters 1-3 is the addition of a slow single-axis gimbal that provides 360° of rotational capability. The net effect of the combined system is that low frequency pointing and disturbance rejection demands are met by this slow gimbal, while the high bandwidth piezo driven system handles the high frequency requirements. A single-axis gimbal is implemented in the form of a DC motor driven turntable. The dual actuator system is integrated by mounting the mirror-piezo assembly on top of this turntable. Angular control can therefore be applied through either the piezo input voltage or the DC motor input voltage. An Electro-Mike displacement transducer is used to detect gimbal angle through the motion of a 6 inch aluminum armature mounted from the turntable's rotating base. Figure 4.1 shows the setup including the mirror-piezo assembly, the turntable, the Electro-Mike, and the DC motor.

### 4.2 *Description of Hardware*

#### 4.2.1 *DC Motor Driven Turntable*

The turntable-DC motor assembly was originally used by Captain Harry Gross at the U.S. Air Force Academy [Gross 90]. It consists of a DC motor and gearbox which are connected to the turntable by a flexible chain. An aluminum chassis houses the entire setup. The gear ratios provide a steady state rate constant of 13.3 (mrad/s)/volt.

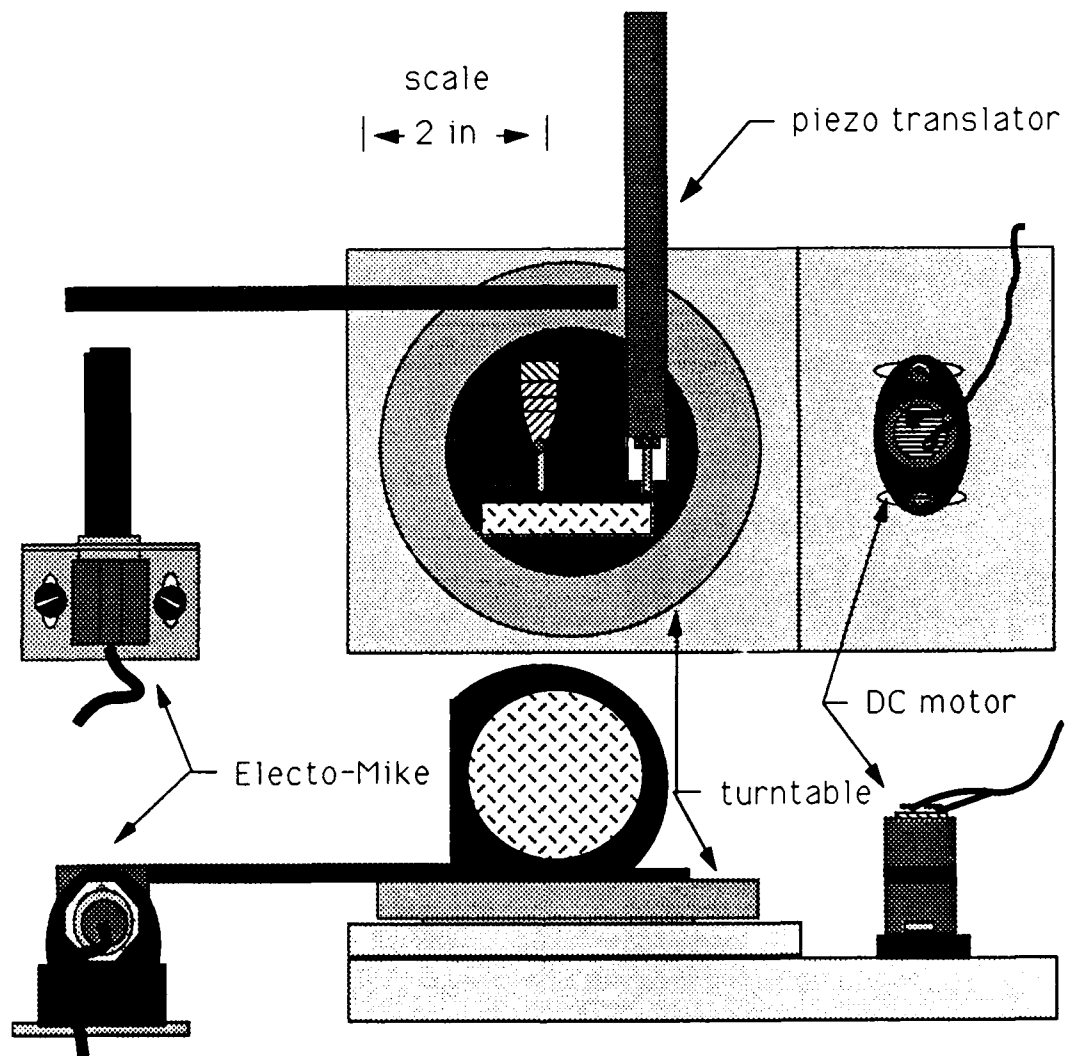


Figure 4.1: Dual Actuator Setup for Mirror Pointing

Because of the nature of the gear-chain linkages in the drive system, near stall and fine positioning performance is poor while speed control is satisfactory.

#### 4.2.2 Displacement Transducer

The Electro-Mike PA12D03 displacement transducer measures the distance between it and a thin steel plate mounted at the tip of the aluminum armature that extends from the turntable (see Figure 4.1). The sensor has a linear position detection range of 0.050 to 0.500 inches. Using the small angle assumption,  $\sin(\Theta) \approx \Theta$ , the position signal can be divided by the armature length to get a  $\Theta_{turntable}$  signal. The Electro-Mike is calibrated such that its output is 0.041 volts/mrad.

#### 4.3 Modeling of the DC Motor Driven Turntable

Modeling the turntable through open loop analysis proved to be difficult because of the neutral position stability of the DC motor. Any test signal used to drive the motor unavoidably contains some DC component. The DC voltage causes the turntable to rotate out of sensor range before sufficient data can be acquired. For this reason a more structured approach to modeling is taken. Initially the form for the transfer function of control voltage input to turntable angle output is assumed to be that of a simple DC motor with a constant to account for gearing.

$$G_{turntable}(s) = \frac{K(1/\tau)}{s(s + (1/\tau))} \quad (4.1)$$

K is the steady state rate constant of 13.3 (mrad/s)/volt. The lag constant  $\tau$  must be determined. Because the turntable plant is difficult to analyze open loop, a closed loop root-locus approach is taken to determine the unknown parameters. The 2630 is not used because it has poor capabilities at frequencies below 1 Hz. Instead a digital storage oscilloscope with an attached X-Y plotter is used for data acquisition. The position signal from the Electro-Mike is sent through a potentiometer and connected to the DC motor driving amplifier. This closed loop setup creates position stability, so the DC signal problem is eliminated. Root locus analysis is carried out by varying the potentiometer setting and estimating the system's natural frequency and damping at each point. The frequency of the response to a step input,  $\omega_d$ , is measured along

with the settling time,  $t_s$ . The natural frequency,  $\omega_n$ , and damping,  $\xi$ , for that point are then determined using the relationships:

$$\omega_n = \frac{\omega_d}{\sqrt{1 - \xi^2}} \quad (4.2)$$

$$\xi \approx \frac{4}{t_s \omega_n}. \quad (4.3)$$

The oscillatory characteristic root locations can then be determined:

$$s = -\xi\omega_n \pm \omega_n\sqrt{1 - \xi^2}. \quad (4.4)$$

This analysis yields a characteristic root loci shown in Figure 4.2.

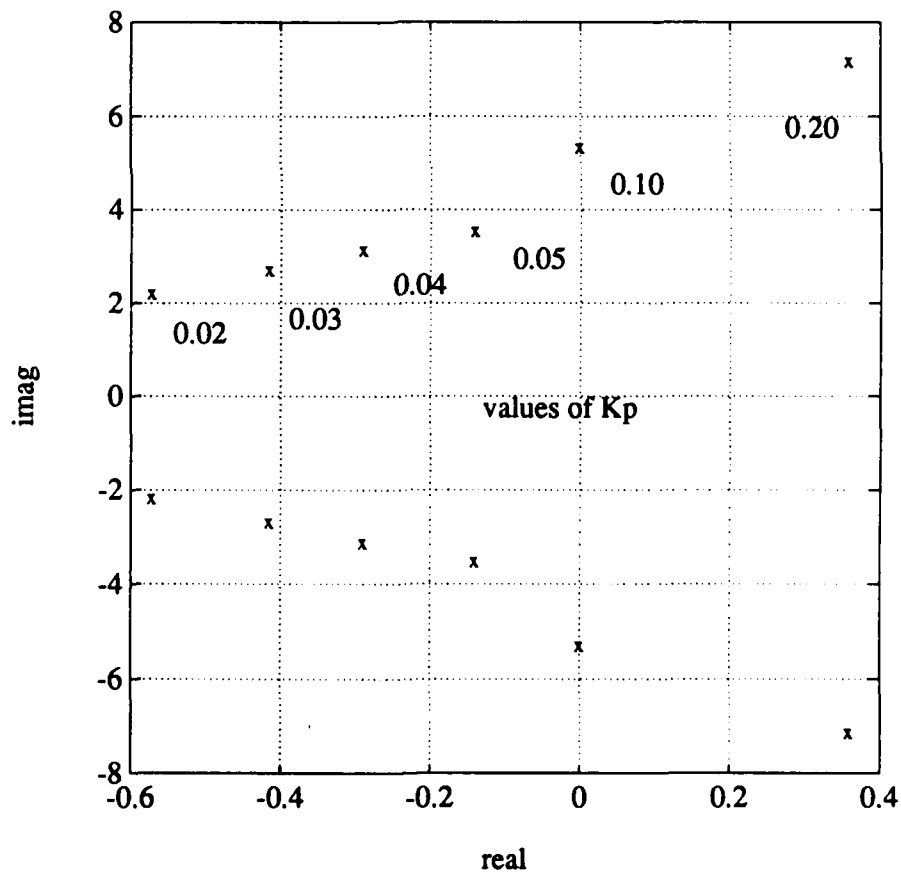


Figure 4.2: Experimental Root Locus for Turntable

The proportional feedback system goes unstable quite quickly for very moderate gains. Such behavior is not well explained by equation 4.1, because the system model never goes unstable under proportional feedback. The problem appears to be a slight time delay in the response of the DC motor and a small amount of play in the flexible chain that connects the motor to the turntable. These effects are lumped together and assumed to act as a dead time,  $T$ . The parameterized turntable model is modified to represent this destabilizing condition.

$$G_{\text{turntable}}(s) = \frac{K(1/\tau)e^{-Ts}}{s(s + (1/\tau))} \quad (4.5)$$

An approximation for the delay term,  $e^{-Ts}$ , can be found to put the transfer function in terms of simple explicit equations. Two methods are attempted: a first order Taylor series approximation,

$$e^{-Ts} = \frac{1}{e^{Ts}} = \frac{1}{1 + Ts + (T^2s^2/2!) + \dots} \approx \frac{1}{1 + Ts} \quad (4.6)$$

and a second order Padé approximation,

$$e^{-Ts} \approx \frac{1 - \frac{T}{2}s + \frac{T^2}{12}s^2}{1 + \frac{T}{2}s + \frac{T^2}{12}s^2}. \quad (4.7)$$

In both cases two parameters,  $\tau$  and  $T$ , must now be determined to find the model. An initial guess for these values is made by examining a step response of the open loop system. Figure 4.3 shows the position output and the step input control voltage. The time delay,  $T$ , is estimated at 0.152 seconds, and the lag constant,  $\tau$ , is guessed at 0.25 seconds. These parameters are tuned until the root locus of the model matches reasonably well with the experimental values. The values lose some physical significance with this tuning, but the resulting model is one that best represents the stability properties of the turntable plant. It turns out that the first order Taylor series approximation for the time delay does just as good a job in representing the time delay as the second order Padé approximation. The first order method is chosen for the sake of simplicity. The final values for the parameters are  $T = 0.050$  and  $\tau = 0.833$ , completing the model.

$$G_{\text{turntable}}(s) = \frac{13.3(1.2)(20)}{s(s + 1.2)(s + 20)} \quad (4.8)$$

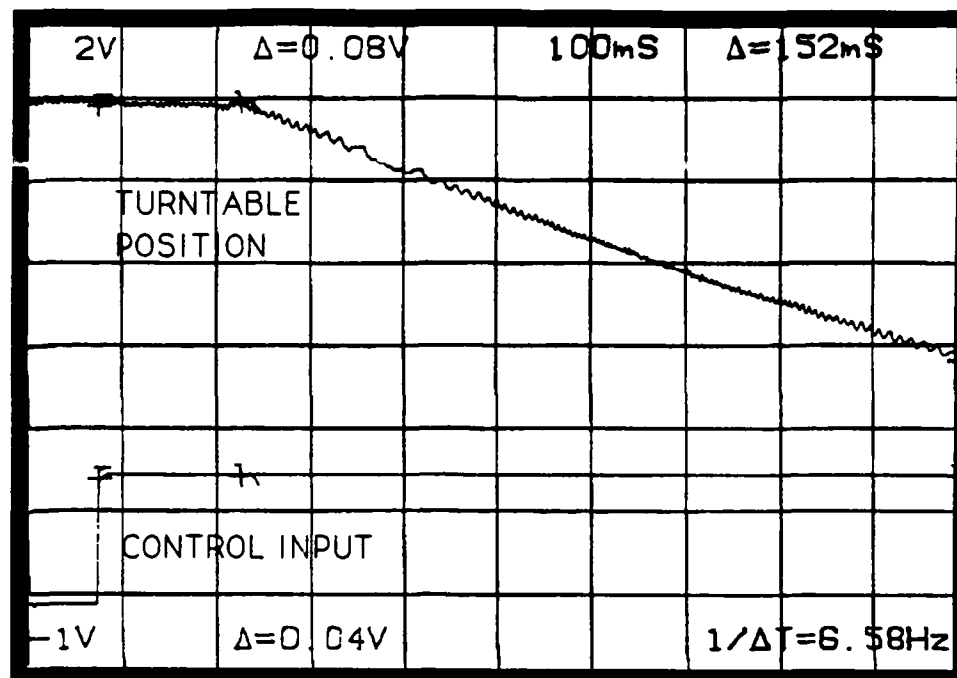


Figure 4.3: Open Loop Turntable Step Response

#### 4.4 Lead Compensation

As Figure 4.2 shows, the DC motor-turntable plant exhibits poor stability characteristics under proportional compensation. The available signal for feedback is  $\Theta_{turntable}$  derived from the Electro-Mike output. The stabilizing signal  $\dot{\Theta}_{turntable}$  is not available as the DC motor is not fitted with a tachometer. The solution is the use of lead compensation to improve response speed and damping. The position transducer signal is fed through an analog computer implemented controller circuit and into the DC motor amplifier. The controller transfer function has the form:

$$G_{lead}(s) = \frac{K_{lead}(s + Z)}{(s + P)} \quad P > Z. \quad (4.9)$$

The implemented values for  $Z$  and  $P$  are 2.00 and 45.5 respectively. Increasing the parameter  $K_{lead}$  raises the natural frequency of the system but decreases damping. A gain of 10.0 provides critical damping and quick time responses. The final lead compensator is:

$$G_{lead}(s) = \frac{10(s + 2)}{(s + 45.5)}. \quad (4.10)$$

The response of the closed loop turntable system to a step command is shown in Figure 4.4. A settling time of 1.25 seconds is achieved with critical damping. The loop gain margin is 8.8 dB, that is  $K_{lead}$  can be increased to 27.6 before the system goes unstable. At gains larger than 10.0, higher order dynamics become a problem. The start of this trend can be seen in Figure 4.4 as the slight pause in the step response at 0.10 seconds.

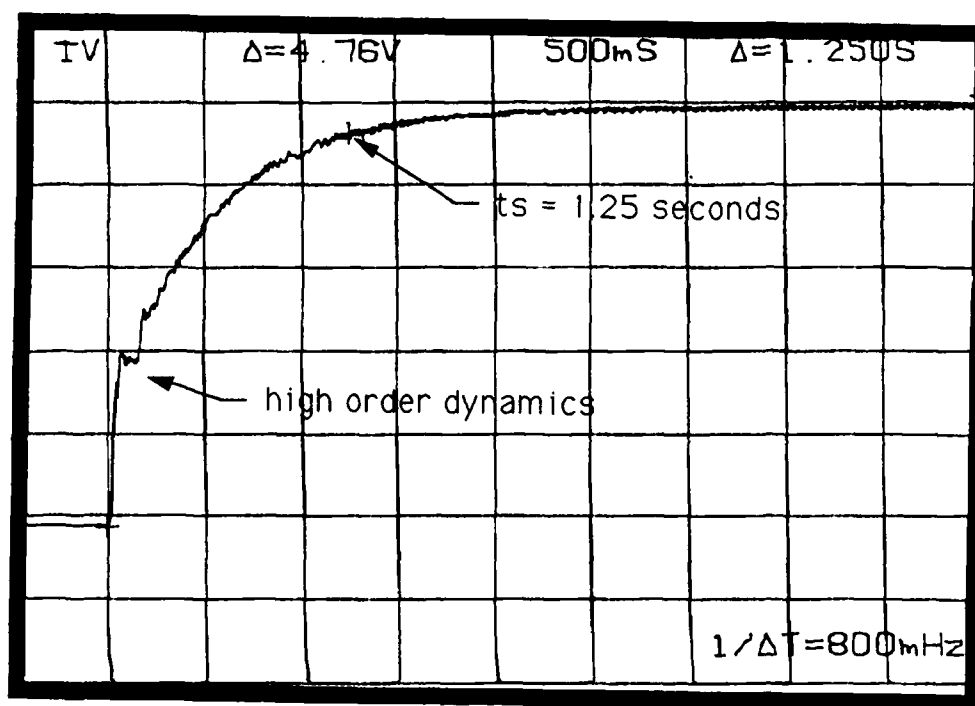


Figure 4.4: Closed Loop Turntable Step Response

#### 4.5 Command Driven Pointing System

A simple configuration for combining the turntable and piezo-mirror in a combined pointing system is the command driven pointing system. The logic behind this setup is that the turntable is directed independently of the piezo-mirror by some external, open loop pointing command. This simulates the use of an outside signal coming from devices such as radar or infra-red tracking systems. The turntable starts from an initial condition that has the beam out of the photodetector range. When the

command is applied, the DC motor drives the turntable to the center of the sensor in approximately 1.25 seconds as shown in Figure 4.4. The piezo-mirror is used for precision pointing and disturbance rejection. While the beam is off of the photodetector, the PI loop of the fast loop rejection system must be disengaged. This requirement exists because without the beam on the sensor, the feedback signal increases to saturate the piezo amplifier and negate the effectiveness of feedforward control. If the sensor feedback is not disengaged, the position error becomes unobservable and any small DC component in the sensor position signal due to asymmetric lighting is integrated without control. Another problem that exists when the beam is not in sensor range is noise. The magnitude of the position signal noise increases greatly when the strong beam illumination is removed, all that is left is the noisy jitter from the AC powered room fluorescent lighting discussed in section 1.3.5. Obviously, when the photodetector is not illuminated by the laser beam, the PI feedback loop must be rendered inoperative. This is done using a DC relay and the sum signal from the sensor. The sum signal, a measure of the magnitude of photodetector illumination, is approximately 0.4 volts without and 5.5 volts with the laser beam on the sensor. This sum signal acts as a trigger which closes the PI loop when its voltage reaches the relay threshold of 2.5 volts. The overall command driven pointing system block diagram is shown in Figure 4.5. With the beam off of the photodetector and the PI loop disengaged, the feedforward controller is still operative. Disturbance rejection therefore follows the curve for feedforward control until the turntable positions the beam on the target, at which point the curve for closed loop with feedforward control applies (see Figure 3.8).

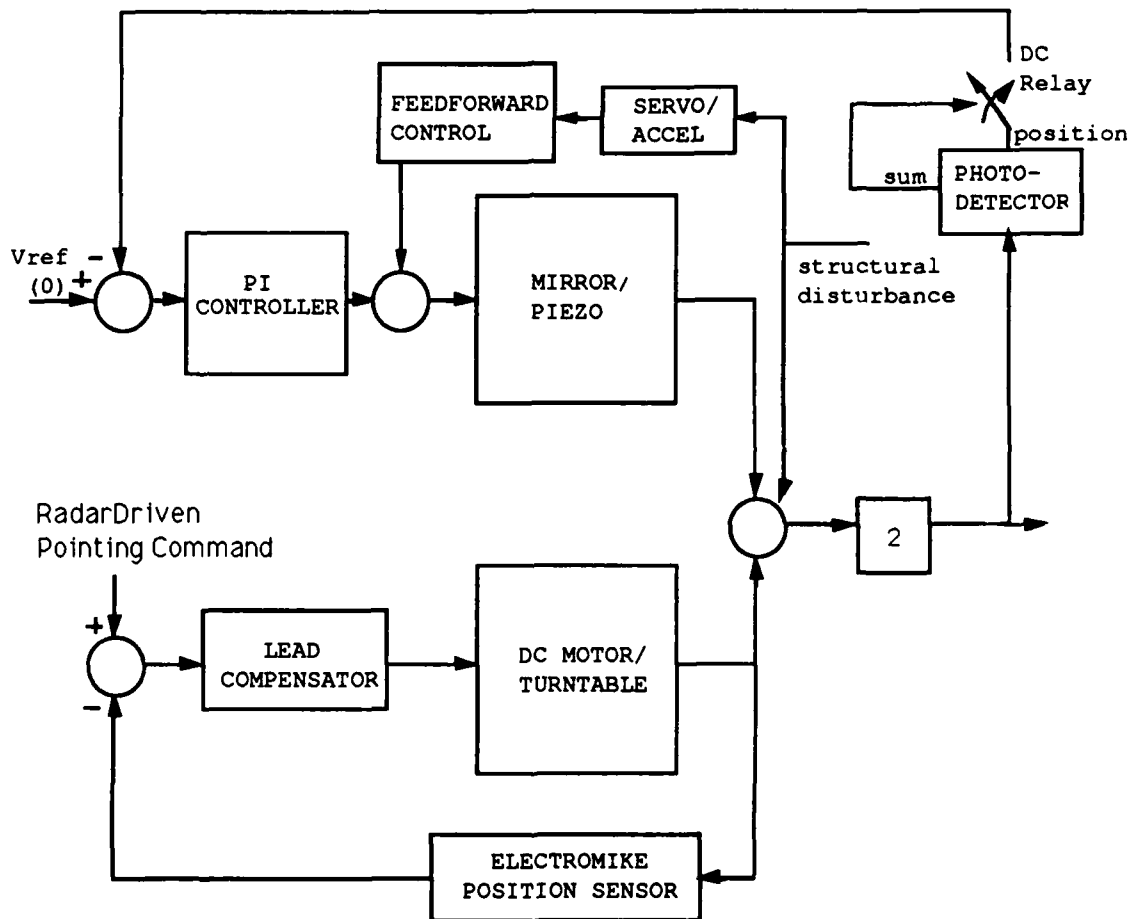


Figure 4.5: Command Driven Pointing System Block Diagram

#### 4.6 Master-Slave Pointing System

A second configuration for the integration of the turntable and the mirror-piezo plants is the master-slave pointing system. Unlike the command driven system, this setup requires that the beam remain on the sensor at all times. The turntable acts as a single-axis gimbal that takes care of the large scale angle and slow disturbance rejection requirements. The piezo-mirror plant takes care of the high frequency, low authority demands on this combined system. Using these two plants to essentially accomplish the same goal but over separate operating bandwidths creates a feedback signal problem. If the sensor position output is used as the driving signal for both actuators, the turntable is rendered useless. In this case the piezo-mirror acts quickly to eliminate any error until its control authority is exhausted. While this condition exists, the slower turntable never has a chance to react. The beam leaves the photodetector range before the piezo translator range is exceeded and when that happens the target becomes unobservable and the system crashes. The solution to this problem is to have the turntable work in a cooperative rather than adversarial relationship with the piezo loop. The lead compensated turntable is *slaved* to the PI controlled piezo loop as shown in Figure 4.6. The output of the PI controller is fed through a crossfeed controller and into the turntable loop as a reference input. In this way an error signal is generated that drives the turntable to *relieve* the piezo translator from its low frequency and DC requirements. The slow loop trails the fast loop and thus the term *slave* and *master*. The crossfeed term is configured as a PI controller of the form

$$G_{crossfeed}(s) = \frac{0.25(s + 0.50)}{s}. \quad (4.11)$$

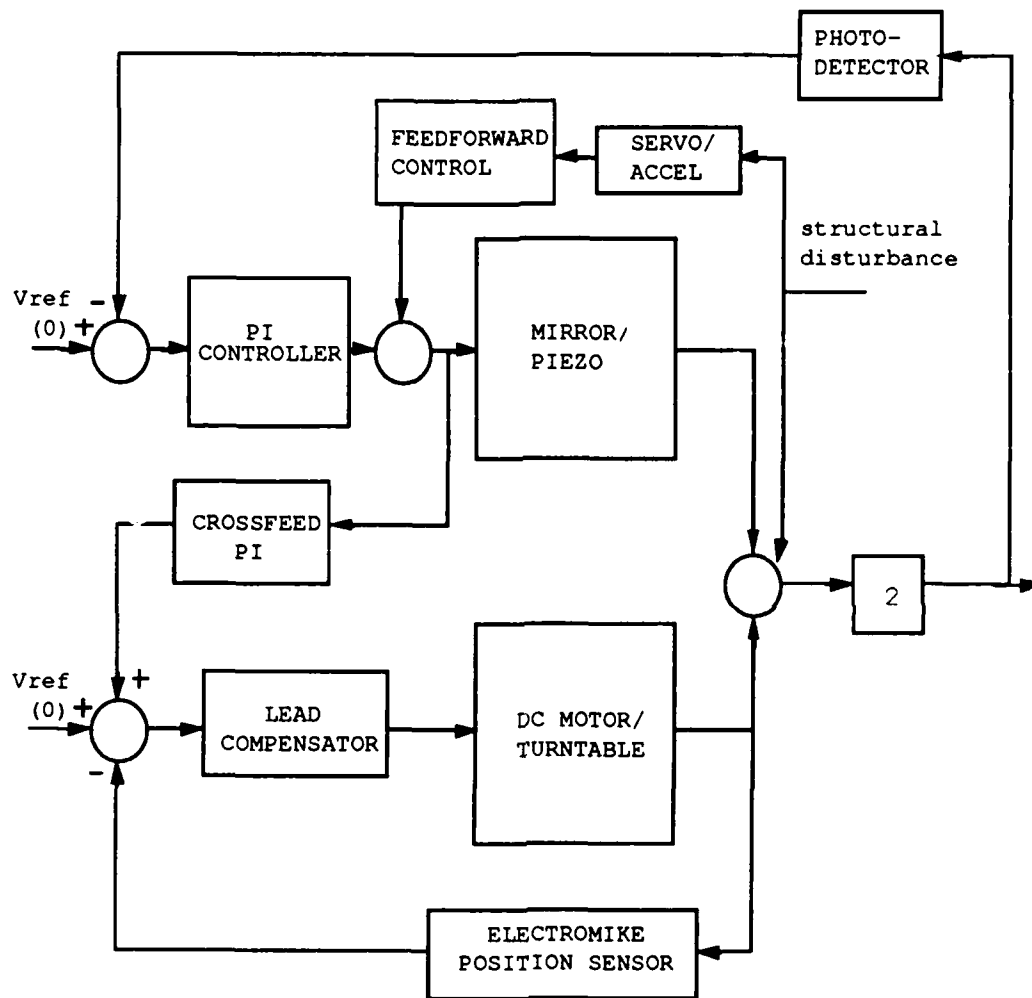


Figure 4.6: Master-Slave Pointing System Block Diagram

The implementation of the crossfeed term is limited by stability problems caused by the non-minimum phase behavior in the DC motor driven turntable. This stability problem is the major limitation of the performance of this master-slaved pointing system. The crossfeed controller presented in equation 4.11 represents the maximum gains and thus maximum pointing performance available while maintaining the stability of the overall system. Figure 4.7 shows the response of the piezo loop PI controller output to a step displacement of the target. The initial jump results from the piezo

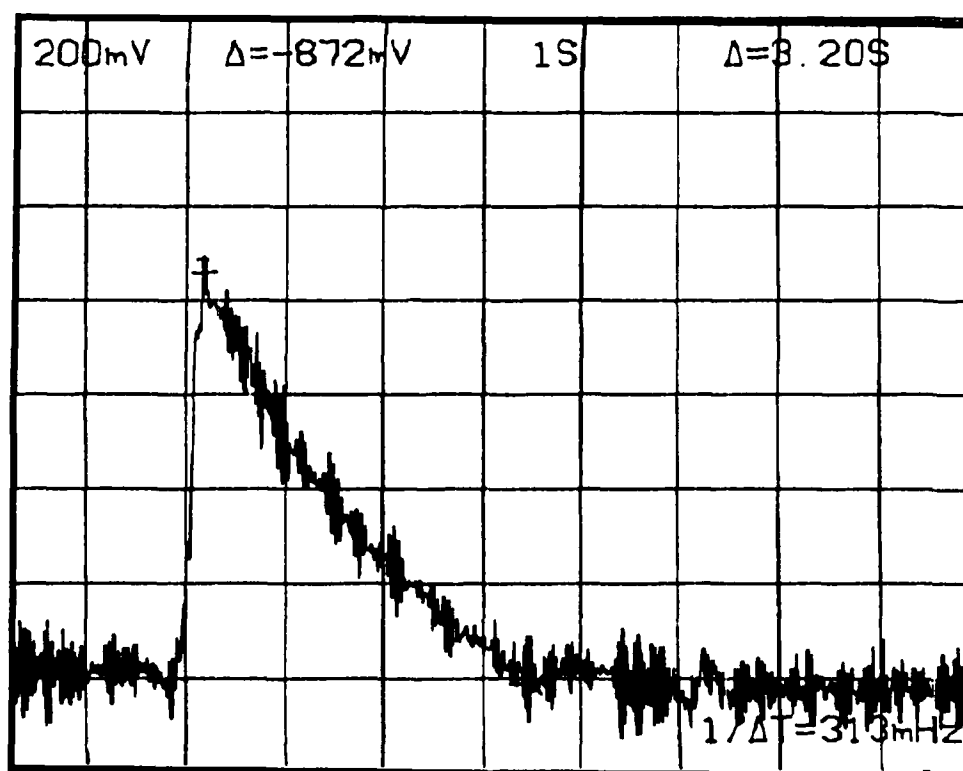


Figure 4.7: Piezo Loop PI Controller Output Voltage Response to Step Target Displacement

quickly eliminating the error signal feedback from the sensor. The exponential decay that follows is the action of the turntable as it *relieves* the piezo translator until in steady state the piezo driving voltage is zero. The steady state turntable driving voltage is also zero because of the position freedom of the DC motor. Notice that the settling time for this step response is large,  $t_s = 3.20$  seconds. Pointing performance

of the master-slave system is slow due to the stability limitations discussed above. The maximum tracking velocity of the implemented setup is 1.01 mrad/second.

## Chapter 5

### **CONCLUSIONS AND RECOMMENDATIONS FOR FUTURE WORK**

Successful design and implementation of a disturbance rejection system for the structurally borne laser beam path has been demonstrated. Both closed loop PI and open loop feedforward control is used to drive the plant, a piezo actuated mirror. The bandwidth of the closed loop system is 60 Hz, a value that represents the compromise between command following-disturbance rejection requirements and signal noise considerations. The feedforward loop provides additional rejection of structural disturbances while not affecting the system bandwidth. Experimental results show that good disturbance rejection is achieved for the first four dominant transverse modes of the 20 bay flexible planar truss structure.

The two pointing systems which make use of the DC motor driven turntable show how slow, large scale motion actuators can be coupled with fast, limited range devices to form an effective hybrid setup. The most restrictive element in the experimental implementation of these systems is the DC motor. It has poor near stall performance and the driving mechanism has characteristic time delays. By adapting a better performing motor such as a direct drive DC unit to this hybrid setup, these problems could be avoided. Improved stability properties would allow much greater latitude in design for achieving a faster two loop pointing system.

While the experimental setup discussed in this thesis is limited to a single degree of freedom mirror, it may easily be expanded to two degrees of freedom by using a second piezo translator mounted in the vertical axis. In this case a dual axis photodetector would be used for feedback in two separate PI control loops. An experimental setup with a two degree of freedom mirror is necessary for most practical pointing and tracking applications. Targets rarely maintain a path along a single axis and flexible structures normally have torsional modes. The single axis experiment serves as a baseline for the more complicated applications, it exposes the major hardware limitations and allows for the exploration of useful control strategies.

## BIBLIOGRAPHY

- [Gross 90] H. N. Gross, E. H. Lechgar, and M. E. Skeen. Development of a Laser Pointing and Tracking System. AAS 90-021, *13th Annual AAS Guidance and Control Conference, Keystone, CO*, February 3-7, 1990.
- [Hallauer 89] W. L. Hallauer Jr. and S. E. Lamberson. Experimental Active Vibration Damping of a Plane Truss Using Hybrid Actuation. AIAA Paper 89-1169, *30th Structures, Structural Dynamics and Materials Conference, Mobile, AL*, April 3-5, 1989.
- [Hughes 86] R. O. Hughes. *Conceptual Design of Pointing Control Systems for Space Station Gimballed Payloads*. AIAA Paper 86-1986, August, 1986.
- [Tektronix 89] Tektronix 2630 Personal Fourier Analyzer Operation Manual, Tektronix Inc., Campbell CA, September, 1989.